Spatially resolved measurements of load current delivery on a 14 MA, 100 ns pulsed power experiment using a line-imaging velocity interferometer

Clayton E. Myers,[1,*] David E. Bliss,[1] Peter M. Celliers,[2] Philip S. Datte,[2] Mark H. Hess,[1]
Christopher A. Jennings,[1] Michael C. Jones,[1] David J. Ampleford,[1] Carlos R. Aragon,[1] Kevin N. Austin,[1]
Thomas G. Avila,[1] Thomas J. Awe,[1] Jacob L. Baker,[1] Ron Bettencourt,[2] Erlan Bliss,[2]
Mark W. Bowers,[2] Neil Butler,[2] John R. Celeste,[2] Todd J. Clancy,[2] Simon J. Cohen,[2] Levi J. Cortez,[1]
Michael K. Crosley,[2] John Edwards,[2] C. Leland Ellison,[2] Jim Emig,[2] David J. Erskine,[2]
William A. Farmer,[2] Jeffrey R. Fein,[1] Dayne E. Fratanduono,[2] Gene Frieders,[2] Justin D. Galbraith,[2]
Jeffrey K. Georgeson,[1] Jeffry W. Gluth,[1] Matthew R. Gomez,[1] James H. Hammer,[2] Roger L. Harmon,[1]
Jose Hernandez,[2] John Jackson,[2] Drew W. Johnson,[1] Brent Jones,[1] Patrick F. Knapp,[1] Don Koen,[2]
Doug Larson,[2] Keith R. LeChien,[2] Michael C. Lowinske,[1] Jeremy Lusk,[2] Keven A. MacRunnels,[1]
Angel N. Martinez,[2] Warren Massey,[2] M. Keith Matzen,[1] Andrew J. Maurer,[1] Tom McCarville,[2]
Robert McDonald,[2] Harry S. McLean,[2] Jerry A. Mills,[1] Leo P. Molina,[1] Michael M. Montoya,[1]
Gregory Natoni,[1] Matthew I. T. Olson,[1] Andrew J. Porwitzky,[1] Kumar S. Raman,[2]
Grafton K. Robertson,[1] Gregory A. Rochau,[1] Samuel Rodriguez,[2] Rodney D. Scharberg,[1]
Daniel J. Scoglietti,[1] Edward Scoglietti,[1] Raymond Shelton,[1] Jonathon E. Shores,[1] Daniel B. Sinars,[1]
Christopher S. Speas,[1] Robert J. Speas,[1] Decker C. Spencer,[1] Paul T. Springer,[2] Eugene Vergel de Dios,[2]
Nathan R. Wemple,[1] Scott E. Winters,[2] J. Nan Wong,[2] and Adam J. York[1]

[1]*Sandia National Laboratories, Albuquerque, New Mexico 87185, USA*
[2]*Lawrence Livermore National Laboratory, Livermore, California 94550, USA*

(Received 1 April 2022; revised 1 May 2023; accepted 8 May 2023; published 24 July 2023)

Pulsed power generators create high-energy-density conditions by rapidly delivering an immense pulse of electrical current to a compact imploding load. Accurately measuring the shape and amplitude of this load current pulse is essential to understanding the behavior of all pulsed power experiments. At the Z Pulsed Power Facility, the closest-in load current measurements are provided by velocimetry techniques such as VISAR (velocity interferometer system for any reflector) and PDV (photonic Doppler velocimetry). Here, fiber-coupled interferometers measure the velocity history of an exploding metallic flyer plate that is embedded in the vertical walls of the current return can. The flyer plate is driven outward by the magnetic pressure from the load current such that magnetohydrodynamic modeling can be used to determine the load current waveform from the measured velocity history. In this paper, we present the first load current velocimetry measurements to be made from the horizontal top flyer plate that carries current radially inward from the return can to the load. These spatially resolved measurements, which span $R = 5$–9 mm, are enabled by a transformative new velocimetry diagnostic—a line-imaging velocity interferometer called Z Line VISAR (ZLV)—whose optical performance overcomes the measurement challenges presented by the steep velocity gradients encountered on the top flyer plate. To validate ZLV's capabilities, a 14-MA, 100-ns experiment was conducted to losslessly couple current up the return can and radially inward across the top flyer plate. Comparisons between the ZLV data obtained from this experiment and two-dimensional magnetohydrodynamic simulations driven with the current measured on the return can indicate that the current delivery across the top flyer plate is indeed lossless to within the few-percent uncertainty of the ZLV data. Given that the current coupling is lossless, the experimental results are used to demonstrate that one-dimensional current unfold techniques can be applied to generate a radially resolved load current map from the ZLV velocity data. This analysis provides a template for how to use the ZLV diagnostic to determine the efficacy of current delivery in future experiments where losses may occur in close proximity to the load.

DOI: 10.1103/PhysRevAccelBeams.26.070401

---

[*] cemyers@sandia.gov
Present address: Commonwealth Fusion Systems, Devens, Massachusetts 01434, USA.

I. INTRODUCTION

The Z machine creates high-energy-density conditions by applying multimegabar magnetic pressures to centimeter-scale imploding loads [1]. These substantial drive pressures are generated by a >20 MA, 100 ns pulse of electric current that flows along the outer surface of the metallic target [2]. The extreme current densities and electric fields associated with this current pulse create charged particles and plasma in the final ~10 cm of the transmission line that can shunt current away from the load region and degrade the electrical power and energy delivered to the target [3–7]. To identify current loss locations and quantify the magnetic pressures that ultimately drive the implosion, it is crucial to measure the electric current both in as many places as possible and as close to the load as possible.

For much of Z's history, the closest current measurements to the load have been made with B-dot sensors at a radius of ~5 cm [8,9]. These measurements work well on loads such as wire arrays where the initial inductance is low and the current delivery is essentially lossless until the late stages of the implosion [10]. In recent years, however, new target concepts such as magnetized liner inertial fusion (MagLIF) [11,12] have increased the prevalence of high-inductance configurations where the power flow conditions are more harsh and current loss can be extensive [13]. The need to quantify the current delivered to the load region on MagLIF and other lossy experiments has recently motivated a multiyear effort to develop a new technique for measuring the current at a radius of ~1 cm on Z: load current velocimetry.

Originally developed on planar [14–16] and cylindrical [17–19] dynamic materials experiments, load current velocimetry has recently been adapted to short-pulse radiation and fusion experiments [20–22]. In a cylindrical configuration, load current velocimetry takes advantage of the fact that the magnetic pressure in the load region acts both to implode the target on-axis and to explode the larger, concentric *return can* that closes the electrical circuit. The current I_{load} that flows axially up the inner surface of the return can applies a magnetic pressure P_{mag} on the return can metal that is given by

$$P_{\mathrm{mag}} = \frac{B_{\mathrm{can}}^2}{2\mu_0} \quad \text{where} \quad B_{\mathrm{can}} \equiv \frac{\mu_0 I_{\mathrm{load}}}{2\pi R_{\mathrm{can}}}. \tag{1}$$

Here, B_{can} is the azimuthal magnetic field on the inner surface of the return can, R_{can} is the return can inner radius, and μ_0 is the magnetic permeability of free space. The drive pressure P_{mag} launches a radially propagating wave that transits through the metal of the return can and eventually breaks out of its outer surface. Following breakout, the return can becomes a cylindrical *flyer plate* that explodes with a free-surface velocity that carries information about the magnetic pressure and therefore the electric current that drove it. If this velocity history can be measured and the properties of the return can material are well characterized (e.g., its equation of state and electrical conductivity), a load current waveform $I_{\mathrm{load}}(t)$ can be numerically *unfolded* from the measured velocity history. Typically, an iterative solver is used to invert the velocity solution that is generated by a one-dimensional magnetohydrodynamic model of the flyer plate that includes its inner radius, thickness, density, equation of state, and electrical conductivity [19,22].

Return-can flyer velocities are routinely measured on Z using two complementary velocimetry systems: VISAR (velocity interferometer system for any reflector) and PDV (photonic Doppler velocimetry). Both are fiber-coupled optical interferometers, but they fundamentally differ in how they convert phase-shifted light reflected from the flyer plate into a velocity measurement. Originally developed by Barker and Hollenbach in the early 1970s [23], VISAR has been a workhorse of dynamic materials research ever since [24,25]. VISAR optically differentiates the laser signal reflected from the flyer plate by splitting the reflected light into two paths, one of which is optically delayed by a glass *etalon* and then mixed with the original signal. The result is a fringe pattern whose phase moves proportionally to the flyer velocity. The velocity sensitivity of the system, or the velocity per fringe (VPF), is determined by the laser wavelength ($\lambda = 532$ nm for the VISAR system at Z) and by the physical properties of the etalon.

PDV, on the other hand, is a displacement interferometry technique that mixes Doppler-shifted light from the moving flyer plate with reference light from a stationary target [26]. With the infrared telecommunications lasers typically used in these systems ($\lambda = 1550$ nm), this signal mixing produces a measurable beat frequency in the gigahertz range that changes proportionally to the velocity of the flyer surface. Since the advent of commercially available high-bandwidth optical amplifiers and digitizers in the early 2000s, PDV has become a workhorse dynamic materials diagnostic in its own right [27]. To make load current velocimetry measurements on Z, single-mode optical fibers for PDV and multimode fibers for VISAR are bundled together into a combined *point probe* that allows both systems to measure the flyer velocity at the same location. At each measurement location, the flyer is diamond-turned to a surface roughness of ~30 nm to maximize reflectivity. This setup enables routine load current velocimetry measurements using both copper and aluminum flyer plates on short-pulse Z experiments [13,20,22].

The fiber-coupled return-can velocimetry techniques described here rely on the assumption that the flyer is driven uniformly along the full height of the measurement region. This assumption typically holds because the vertical walls of the return can reside at a constant radius. As such, so long as the axial current flow along the return can is lossless, all portions of the flyer will be driven by the same magnetic pressure [see Eq. (1)]. To obtain velocimetry-based current measurements between the return can and the load, velocity data must be acquired from the horizontal *top flyer plate* along which the current flows radially inward to the load. Measurements on the top flyer plate are challenging because the flyer is no longer driven uniformly across the measurement region. This is due to both the $1/R^2$ variation in the magnetic drive pressure and the increased likelihood of current loss close to the dynamically imploding load. Such effects can generate steep spatial gradients and non-negligible surface tilts that can quickly compromise fiber-coupled point probes given their finite spot sizes and limited numerical apertures. Top-flyer-plate current measurements are therefore best made by a more advanced velocimetry diagnostic: a line-imaging velocity interferometer, also known as line VISAR.

Line VISAR is an extension of the VISAR concept wherein the evolution of a spatially resolved image of the VISAR fringe pattern is observed. More specifically, the image is recorded using a *streak camera* that generates an image with one spatial dimension and one temporal dimension. As such, the fringe pattern that is projected on the streak camera is actually a linear cut across a two-dimensional image of the flyer plate (hence the name *line* VISAR). Streak cameras were first used to record VISAR fringes in a system called ORVIS (optically recorded velocity interferometer system) [28,29]. ORVIS is a non-imaging configuration that takes advantage of the high-speed recording capabilities of streak cameras to enhance the temporal resolution of a conventional VISAR system. Imaging line VISAR systems with spatial discrimination are a natural evolution of the ORVIS concept. Here, a lens and open-beam transport system are used to project an image of the flyer plate onto the streak camera. Line VISAR systems have been widely utilized to diagnose shock physics experiments on pulsed power [30–34], laser [35–39], and gas gun [40–44] facilities. This broad implementation of line VISAR has generated technological advancements, particularly with the systems at the National Ignition Facility [37,38], that have recently been incorporated into the design of a new line VISAR system at the Z Pulsed Power Facility called Z Line VISAR [45,46]. This system was expressly built to measure the current delivered very close to the load.

In this paper, we describe the first use of Z Line VISAR (ZLV) to make radially resolved load current measurements on a Z experiment. These measurements were acquired on a 14MA, 100 ns validation experiment that was specifically designed to losslessly couple current from the return can across the top flyer plate to the load. Section II describes the experimental setup and the alignment and tuning of the ZLV diagnostic prior to this experiment. Section III presents the ZLV interferograms obtained on the lossless validation experiment and describes the analysis procedure that is used to convert the recorded fringe motion into a velocity map. Section IV presents comparisons between the ZLV velocity data and two-dimensional magnetohydrodynamic simulations driven with the current measured on the return can. These comparisons indicate that current delivery across the top flyer plate is lossless to within the few-percent uncertainty of the ZLV data. Section V introduces the one-dimensional current unfold techniques of Jennings [22] and demonstrates that they can be used to generate a radially resolved load current map from the ZLV velocity data. Establishing this methodology is crucial for interpreting future experiments where the current coupling may not be lossless. Finally, Sec. VI compares the ZLV data obtained on the experiment to complementary top-down point probe data. The limitations of the point probes in this geometry illustrate the groundbreaking capabilities of the ZLV diagnostic.

II. EXPERIMENTAL SETUP

In this section, we introduce the load hardware configuration for the 14MA, 100 ns lossless validation experiment that was specifically designed to provide constraining data

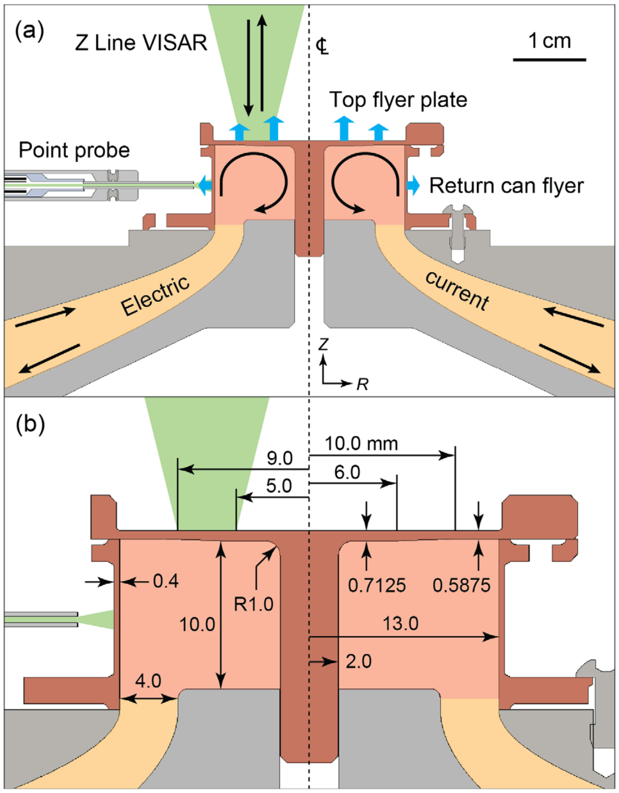

FIG. 1. Load hardware configuration for the 14 MA, 100 ns lossless experiment used to validate the performance of Z Line VISAR. (a) The coaxial load region (salmon-colored) is bounded by a copper return can and top flyer plate that carries current to a solid copper rod on axis (brown). A fiber-coupled point probe (left) and Z Line VISAR (top) are used to measure the magnetically driven explosion of the return can and top flyer plate, respectively. (b) Dimensions of the load region and flyer plates. See the text for further details.

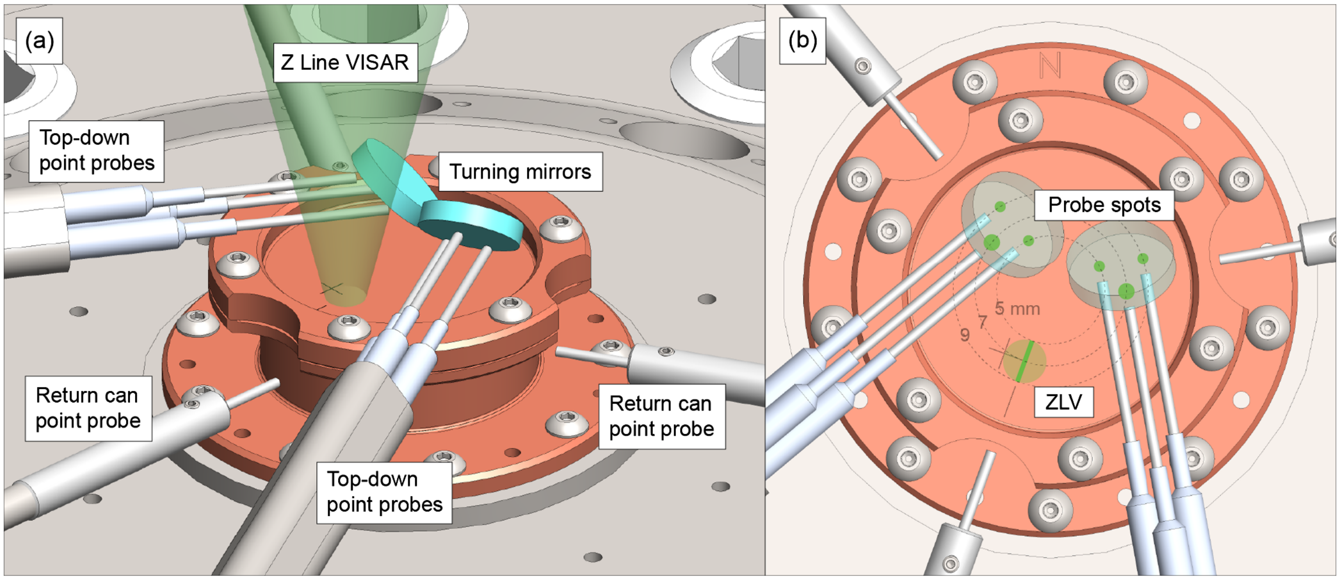

FIG. 2. (a) Isometric and (b) top-down views of the velocimetry diagnostic configuration for the Z Line VISAR (ZLV) validation experiment. The ~14° ZLV beam cone is projected onto the top flyer plate by an $f/2$ final lens. The beam spot spans $R = 5$–9 mm and is located 200° clockwise from North. Two triplets of top-down point probes are directed onto the top flyer plate by turning mirrors located at 80° and 320° clockwise from North. Each triplet provides measurements at $R = 5$, 7, and 9 mm to facilitate direct comparisons to the ZLV data. Finally, three return can probes are oriented at 80°, 200°, and 320° clockwise from North to provide side-on return-can current measurements at each of the top-down measurement locations.

for the ZLV system. We then describe the preshot alignment and tuning of the ZLV diagnostic that is required before each experiment. Figure 1(a) shows that electric current is delivered to the load region (salmon-colored) by the final transmission line (yellow). A 4 mm anode-cathode gap at the base of the load region opens into a 10 mm-tall cylindrical cavity where the current is carried up the return can walls at $R = 13$ mm, inward across the underside of the top flyer plate, and down the 4 mm-diameter solid rod on axis. The return can, top flyer plate, and on-axis rod are all made of copper, which is chosen for its relatively well-constrained equation of state and conductivity. The thickness of the return can is 400 μm, while the thickness of the top flyer plate tapers from 712.5 to 587.5 μm over $R = 6$–10 mm. This taper is necessary to mitigate the tilt of the flyer surface that is generated by the radial magnetic pressure gradient driving the underside of the flyer. Here it is important to limit the surface tilt to $\lesssim 10°$ to ensure that the reflected laser light is collected by the $f/2$ ZLV lens. Figure 1(b) provides detailed dimensions of the load region and the flyer thicknesses used in this experiment. The return can and the top flyer plate together create a fully enclosed load region that maximizes the chance for symmetric current delivery and high-quality velocimetry data return. Furthermore, the ample dimensions of the load region and the nonimploding on-axis rod ensure that load current delivery will be lossless in this experiment.

The uniform radial expansion of the return can flyer at $R = 13$ mm is measured by fiber-coupled point probes that contain both single-mode PDV fibers and multimode VISAR fibers. A cross section of one such probe is depicted on the left side of Figs. 1(a) and 1(b). Under the assumption that the current coupling in this experiment is lossless within the load region, the load current that is measured by the point probes will match the current flowing across the underside of the top flyer plate. The nonuniform explosion of the top flyer plate is measured over $R = 5$–9 mm by the ZLV diagnostic, which is depicted in Fig. 1 as a green beam cone. Figure 2(a) shows a three-dimensional rendering of the ZLV beam cone impinging on the top flyer plate. Alignment fiducials are laser etched into the top surface of the flyer plate, which itself is diamond turned to a surface roughness of ~30 nm so that it acts as a specular reflector for the ZLV beam. The ZLV field of view is 4 mm in diameter.

Also visible in Fig. 2(a) are the numerous side-on and top-down point velocimetry probes that were fielded on the ZLV validation experiment. Three return-can point probes were fielded at 120° increments (two of which are labeled in Fig. 2(a) while the third is visible behind the ZLV beam). This distribution of return-can probes provides an assessment of the symmetry of load current delivery. In addition to the three return-can probes, two triplets of top-down point probes were fielded to provide direct points of comparison to the top-down velocity data obtained by ZLV. The top-down point probe triplets, which each provide measurements at $R = 5$, 7, and 9 mm, are oriented horizontally in the load hardware so that they do not interfere with the ZLV beam cone. Their lines of sight are directed downward onto the top flyer plate by the two

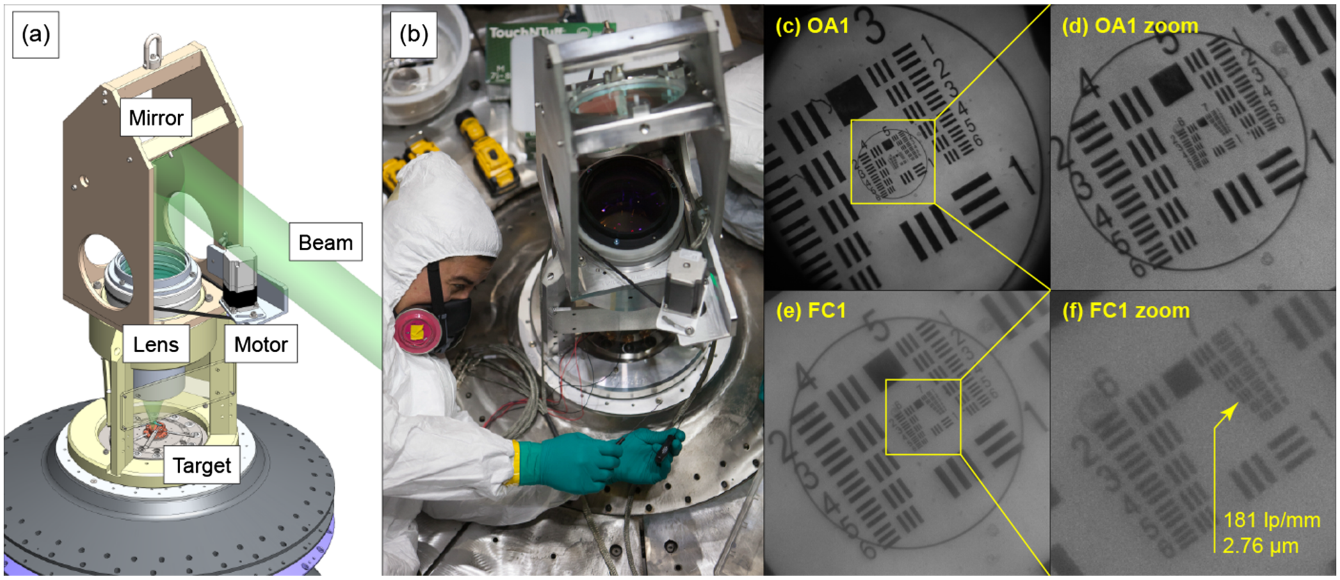

FIG. 3. (a) Rendering and (b) photograph of the installed ZLV final optics assembly (FOA). The FOA contains the consumable final mirror and final lens in the ZLV open-beam transport system. Remote focusing of the final lens is enabled by a stepper motor. Pointing and centering of the beam is achieved by manipulating a coupled pair of mirrors located just outside of the Z vacuum chamber wall. (c)–(f) Orientation-align (OA) and fringe contrast (FC) camera images of a USAF 1951 resolution target placed in chamber. These cameras are located on the ZLV optical table in the remote ZLV diagnostic room. The field of view of the full FC1 image in (e) roughly corresponds to that of the enlarged OA1 image in (d). The enlarged FC1 image in (f) indicates that the ZLV transport system achieves an as-built optical performance of 181 lp/mm or 2.76 μm.

first-surface turning mirrors depicted in light blue in Fig. 2(a). The complete azimuthal distribution of velocimetry diagnostics on the ZLV validation experiment is shown in Fig. 2(b). ZLV is located 200° clockwise from North. The bold green line along which the velocity is measured is oriented radially and spans $R = 5$–9 mm. The two triplets of top-down point probes are located at 80° and 320° clockwise from North. The spot size of each top-down probe depends on the path length from the probe tip to the top flyer plate (see Sec. VI for more information). Finally, the three side-on return-can probes are oriented at 80°, 200°, and 320° clockwise from North to provide a return-can current measurement at each of the top-down measurement locations.

The ZLV beam is relayed to and from the target by a 50m, 12-mirror, 9-lens open-beam transport system that was newly built for ZLV. All but the final mirror and final lens are located outside of the Z vacuum chamber. The optical design [45] and implementation [46] of the ZLV transport system are documented elsewhere, so in this paper, we only describe the components that are manipulated to align and focus the ZLV diagnostic on each experiment. Figure 3(a) illustrates the in-chamber final optics assembly (FOA) that directs and focuses the ZLV beam onto the target. This FOA houses the final mirror and final lens in the transport system. The final mirror directs the beam down through the lens and onto the target. The final lens is a custom six-element $f/2$ lens whose wide range of collection angles enables it to handle the steep radial gradients and surface tilts associated with top-flyer-plate velocimetry. The tight spatial tolerances between the FOA optical elements and the target are achieved by mounting the precision-machined FOA directly to the top anode (to which the target is also mounted). As such, the only adjustment available in chamber is motorized focusing of the final lens. This enables refocusing under vacuum and crucially when some targets are filled with a cryogenic window material such as liquid deuterium [47–49]. A photo of the installation of the FOA that was used in the ZLV validation experiment is shown in Fig. 3(b). The final optics are consumed in each experiment due to their proximity to the exploding load hardware. A transparent blast window at the vacuum chamber wall is also consumed and replaced.

Pointing and centering of the ZLV beam is achieved by manipulating a coupled pair of transport mirrors that is located just outside of the Z vacuum chamber [46]. These mirrors control the centering of the beam on both the final transport mirror and the final transport lens. Iterative manipulation of the coupled mirrors results in a beam that is centered on the target and travels vertically downward from the final mirror through the final lens. Fiducials are scribed on the surface of the target to facilitate pointing, centering, and focusing. This process takes roughly 30 min during a typical ZLV experiment.

The as-built optical performance of the ZLV transport system has been characterized by placing a USAF 1951 resolution target in chamber. Figures 3(c)–3(f) show images of the resolution target taken by the orientation-align (OA) and fringe contrast (FC) cameras that are located in the remote ZLV diagnostic room. The orientation-align camera captures the full 4-mm field of view of the ZLV beam, while the higher-resolution fringe contrast camera captures only a ~1-mm field of view in the center of the resolution target. The enlarged FC1 image in Fig. 3(f) indicates a remarkable as-built optical resolution of 181 lp/mm or 2.76 μm, which is close to the diffraction limit of this $\lambda = 532$ nm, $f/2$ system. Note that 2.76 μm is the resolution of the transport system rather than that of the streaked interferograms, which are degraded to a resolution of 10–70 μm by the achievable fringe density and by additional relay optics and instrument response considerations. Note also that the resolution target images shown in Figs. 3(c)–3(f) were obtained on a later ZLV experiment rather than on the validation experiment discussed in this paper. This was due to time constraints encountered during the execution of the validation experiment. We expect that the optical performance measured here also applies to the validation experiment given that the transport system was not subsequently modified.

Figure 4 shows the alignment of the ZLV beam to the target for the ZLV validation experiment. Figure 4(a) shows the region of interest [enlarged from Fig. 2(b)]. Figure 4(b) shows an LED-illuminated target image after initial pointing, centering, and focusing have been achieved. The laser-etched + fiducial on the left side of the field of view is clearly visible in this dark-field image. Small scratches on the target surface indicate that a high-quality focus has been achieved. Figure 4(c) shows alignment fringes in the same field of view. A green box marks the line along which the streaked interferograms will be recorded. Note that the fringes are oriented orthogonally to this line. Finally, Fig. 4(d) shows a laser-illuminated image of the final target alignment. The illumination is provided by an eye-safe alignment laser that is coupled to the same fiber launch as the pulsed probe laser that illuminates the target during the experiment. In Fig. 4(d), the right edge of + fiducial is aligned to the left edge of the innermost circle on the black alignment reticle. This reticle is located on the ZLV interferometer table and is projected onto the alignment images at 4× magnification such that the 4, 8, and 12 mm circle diameters correspond to 1, 2, and 3 mm on target. The table reticle is removed for the downline experiment.

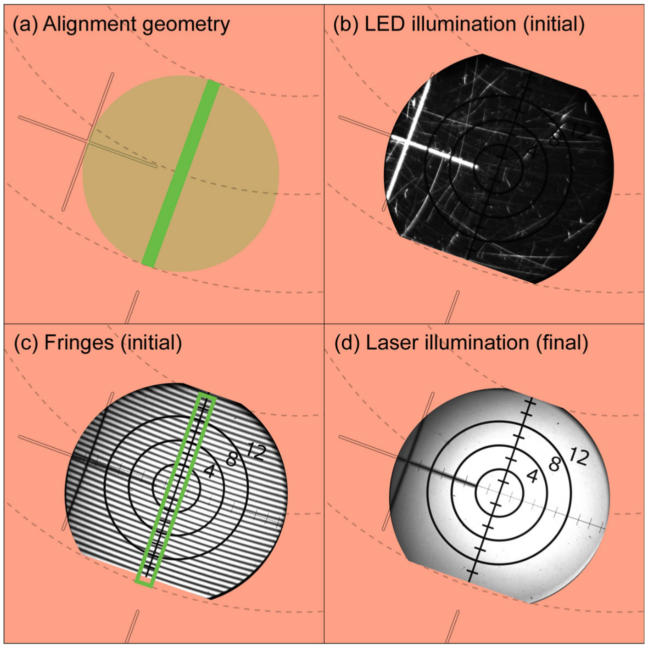

FIG. 4. Alignment of the ZLV beam to the downline target. (a) Diagram of the ZLV field of view and streak line relative to the fiducials etched on the target [enlarged from Fig. 2(b)]. (b) LED-illuminated image after initial pointing, centering, and focusing. (c) Alignment fringes in the same field of view. The green box indicates the streak line. (d) Laser-illuminated image showing the final target alignment with the right edge of the + fiducial aligned to the left edge of the smallest circle on the table reticle. See the text for further details.

Once target alignment has been achieved, preshot interferograms are recorded. This is accomplished by launching the 10 mJ, 100 ns ZLV probe laser ($\lambda = 532$ nm) from the remote ZLV diagnostic room to the target and recording the light that is reflected back through the transport system and onto the ZLV interferometer table. Once it arrives at the table, the reflected light is split between two nominally identical interferometer legs and recorded on two separate Sydor ROSS 5800 streak cameras [50]. The two independent interferometer legs facilitate the use of different etalons (i.e., velocities per fringe) and/or streak fields of view on the same experiment. Using two different etalons can help to resolve fringe ambiguities encountered at shock fronts in the velocity data (see Sec. III). Regarding the streak fields of view, two selections are available for each leg: (i) the spatial extent of the streak line; and (ii) its azimuthal orientation within the ZLV beam cone. For the spatial extent, full field-of-view (FFOV) optics modules are available to project a 1, 2, or 4 mm portion of the ZLV image onto each streak camera. Smaller fields of view yield higher spatial resolutions. For the azimuthal orientation, a K-mirror is embedded in each interferometer leg to independently select the azimuthal orientation of the streak line within the circular ZLV image [45,46]. Azimuthally aligning the fields of view ensures that the same target motion is being recorded on each leg while crossing the fields of view provides an assessment of symmetry when the ZLV image is centered over the target. The interferometer leg and streak camera parameters chosen for the ZLV validation experiment are listed in Table I. We note here that the ZLV system also includes an eight-frame gated optical imager (GOI) that records snapshots of the 2D ZLV field of view [46]. This system is primarily intended to assess the symmetry of experiments where the shock front is energetic enough to generate visible self-emission. While the GOI

TABLE I. Interferometer and streak camera settings for the ZLV validation experiment. The effective spatial resolution is set here by the fringe density (i.e., the number of fringes across the slit). Subsequent ZLV experiments have used a higher fringe density of 50 fringes across the slit to increase the effective spatial resolution. The streak line orientation is quoted in degrees clockwise from North. The full range of available ZLV configurations can be found in Datte *et al.* [46].

Parameter	Leg 1	Leg 2
Full field of view (FFOV)	4 mm	4 mm
Radius at FFOV center	7 mm	7 mm
Fringes across the slit	30	30
Effective spatial resolution	67 μm	67 μm
Sweep speed (streak duration)	64 ns	80 ns
Effective temporal resolution	0.19 ns	0.24 ns
Streak line orientation	20° ↔ 200°	20° ↔ 200°
Velocity per fringe (VPF)	0.989 km/s	0.660 km/s

did not generate data on the ZLV validation experiment, it has subsequently been used to great effect for multiple self-emission imaging applications that will be reported elsewhere.

Figure 5 shows preshot interferograms recorded from each of the ZLV interferometer legs using the settings in Table I. Here, the native space-time distortion of the streak cameras has been corrected using the Sydor DynaCal calibration capability [51]. The spatial registration of each camera is determined by acquiring additional preshot streak images with the fringes blocked and the table reticle in the field of view. The ticks of the table reticle appear as horizontal lines in the streak images that can be tracked to determine the spatial registration of the camera. The temporal registration of the image is acquired from the 0.5-GHz timing combs that are visible at the bottom of the Leg 1 preshot interferogram in Fig. 5(a). Note that, while the two interferograms cover different temporal ranges based on the streak camera settings (64 ns on Leg 1 versus 80 ns on Leg 2), they are cropped in Fig. 5 to a ∼64 ns window. The streak images are registered to the global Z time base with an accuracy of ±1 ns by recording the output of the high-voltage ramp circuits that are embedded in each streak camera. Fine adjustments were made here to reconcile the ZLV time base with that of the point velocimetry systems. Optical fiducials have since been added to further improve the timing accuracy. The fringe amplitude and contrast for each interferometer leg are shown in Fig. 5(c). While the fringe amplitude and contrast are lower than desired, they were deemed to be sufficient for the validation experiment to proceed. As we will show in Sec. III, the fading fringes on the small-radius side of the Leg 2 interferogram proved to be problematic in the downline experiment. This did not, however, prevent the validation experiment from meeting its objectives.

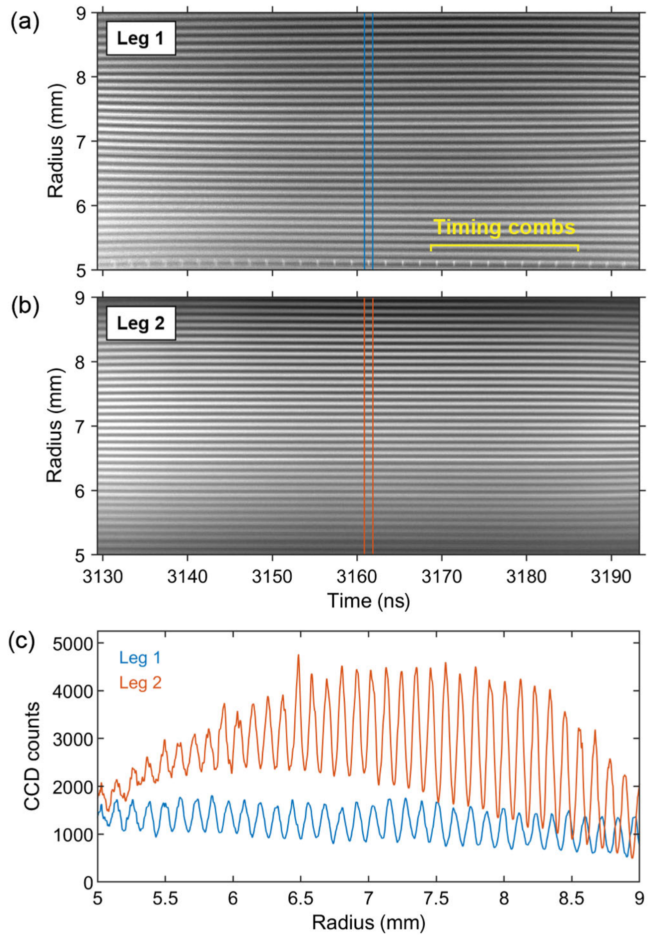

FIG. 5. Preshot interferograms from the (a) Leg 1 and (b) Leg 2 ZLV interferometers. The native space-time distortion of the streak cameras has been corrected in these images. The 0.5-GHz timing combs are visible on the bottom of the Leg 1 interferogram. See the text for further details on the spatial and temporal registration of the streak images. (c) Vertical lineouts at $t \sim 3160$ ns showing the fringe amplitude and contrast in each interferogram.

Fortunately, numerous adjustments to the system have greatly improved the fringe amplitude and contrast in subsequent experiments. The two most impactful adjustments were (i) a realignment of the relay optics that project the fringes onto the streak cameras; and (ii) the inclusion of a laser line filter to suppress stray light generated during the experiment.

III. Z LINE VISAR EXPERIMENTAL RESULTS

On the ZLV validation experiment (Shot z3337), the Z machine was used to drive the load hardware described in Sec. II with a ∼14 MA, 100 ns pulse of current. As expected, the magnetic pressure in the load region launched the top flyer plate of the target upward along the ZLV line-of-sight, and the phase-shifted laser light reflected from the moving flyer plate was successfully recorded on both ZLV

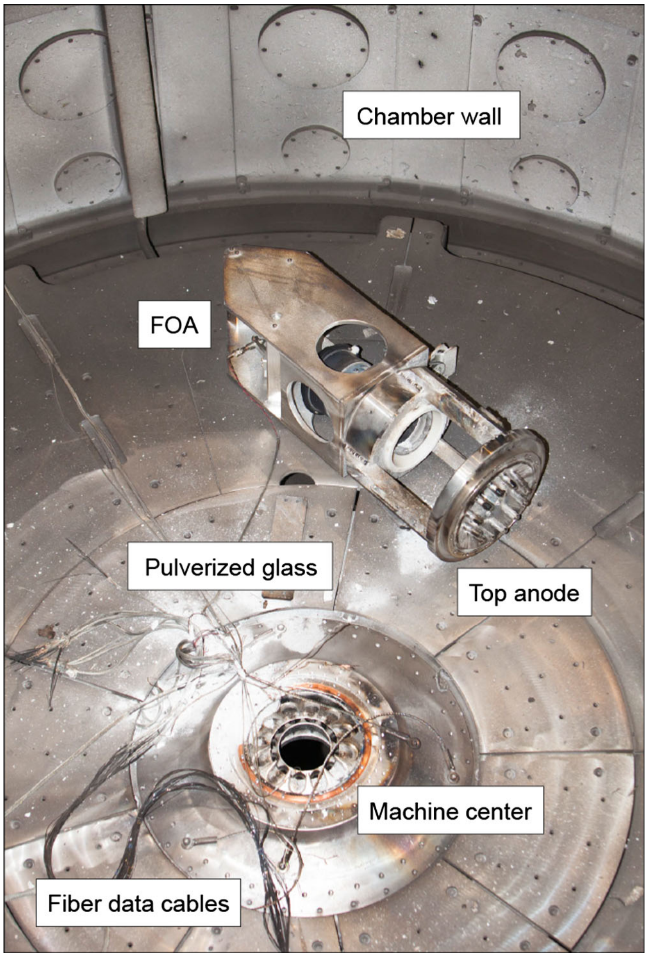

FIG. 6. The postshot debris field created by the ZLV validation experiment (z3337). The ZLV FOA and top anode, which were originally located at machine center, were blown backward by the >1 MJ of electromagnetic energy that is delivered to the load region during the experiment. The white powder that is strewn between machine center and the FOA is pulverized glass from the shattered $f/2$ lens. The remnants of the fiber optic data cables from the point velocimetry probes are visible in the bottom left.

interferometer legs. Ultimately, the >1 MJ of electromagnetic energy delivered to the center of the machine disassembles the load hardware, shatters the $f/2$ final lens, and displaces the ZLV FOA within the Z vacuum chamber. The debris field from the ZLV validation experiment is shown in Fig. 6. This amount of postshot damage, which is to be expected, underscores why the ZLV final optics must be replaced after each experiment.

Figure 7 shows the two raw interferograms recorded on the ZLV validation experiment as well as the various stages of data reduction that are required to extract spatially resolved velocity maps from the raw data. Each column in Fig. 7 represents one of the two ZLV interferometer legs. In the raw interferograms [Fig. 7(a)], the fringes shift discontinuously along a curved shock breakout feature that is highlighted in red. The timing of shock breakout at each spatial location depends both on the magnetic pressure driving the flyer and on the thickness of the flyer at that location, both of which vary with radius. After the shock breakout, the fringes curl downward, indicating that the top flyer plate continues to accelerate throughout the experiment.

Numerous data reduction techniques have been developed to process line VISAR interferograms and convert the recorded fringe motion into spatially resolved velocity maps. These include fringe tracking [52], quadrature approximations [31,40], Fourier transform methods [36,53–55], and continuous wavelet transforms [56,57]. Philpott *et al.* [44] present a detailed comparison of these different approaches. More recently, advanced techniques to address laser speckle [58] and highly spatially varying data [59] have been implemented in an analysis framework that constructs a forward model of the VISAR interferometer [60]. In this paper, we use the Fourier transform method of Celliers *et al.* [36] to extract spatially resolved velocity maps from the raw interferograms. Here, a one-dimensional Fourier transform is applied at each time step to obtain a spatial power spectrum of the information encoded in the interferogram. A bandpass filter is then used to isolate the crucial phase information that is carried by the fringes from the slowly varying background of the streak image. Once the fringes have been isolated in frequency space, an inverse transform is applied to generate a wrapped phase function that contains only information associated with the phase of the fringes as a function of time and space. To complete the analysis, the wrapped phase function is unwrapped and the linear phase ramp from the background fringe pattern is subtracted. This yields an unwrapped phase map where changes in the phase are directly proportional to the flyer velocity. The final velocity map is obtained by scaling the unwrapped phase map by the VPF factor, which is determined by the phase delay introduced by the etalon in each interferometer leg.

Figures 7(b)–7(d) show three different products of the Fourier transform data reduction method. First, Fig. 7(b) shows the normalized fringe patterns obtained from the Fourier transform method. These images, which are generated by subtracting the low-frequency background from the raw interferograms, reveal the shock breakout feature and the subsequent fringe motion much more clearly than the raw interferograms in Fig. 7(a). Figure 7(c) shows the root-mean-square fringe amplitude extracted by transforming and bandpass filtering each interferogram. A low but usable fringe amplitude of ∼300 counts is present across the Leg 1 interferogram, while a more variable fringe amplitude ranging from ∼800 counts to nearly zero is present in Leg 2. The noise floor associated with these low fringe amplitudes slightly increases the uncertainty in the velocity measurements obtained in this experiment. Greatly improved fringe amplitudes in the thousands of counts have been achieved in subsequent ZLV experiments. Finally,

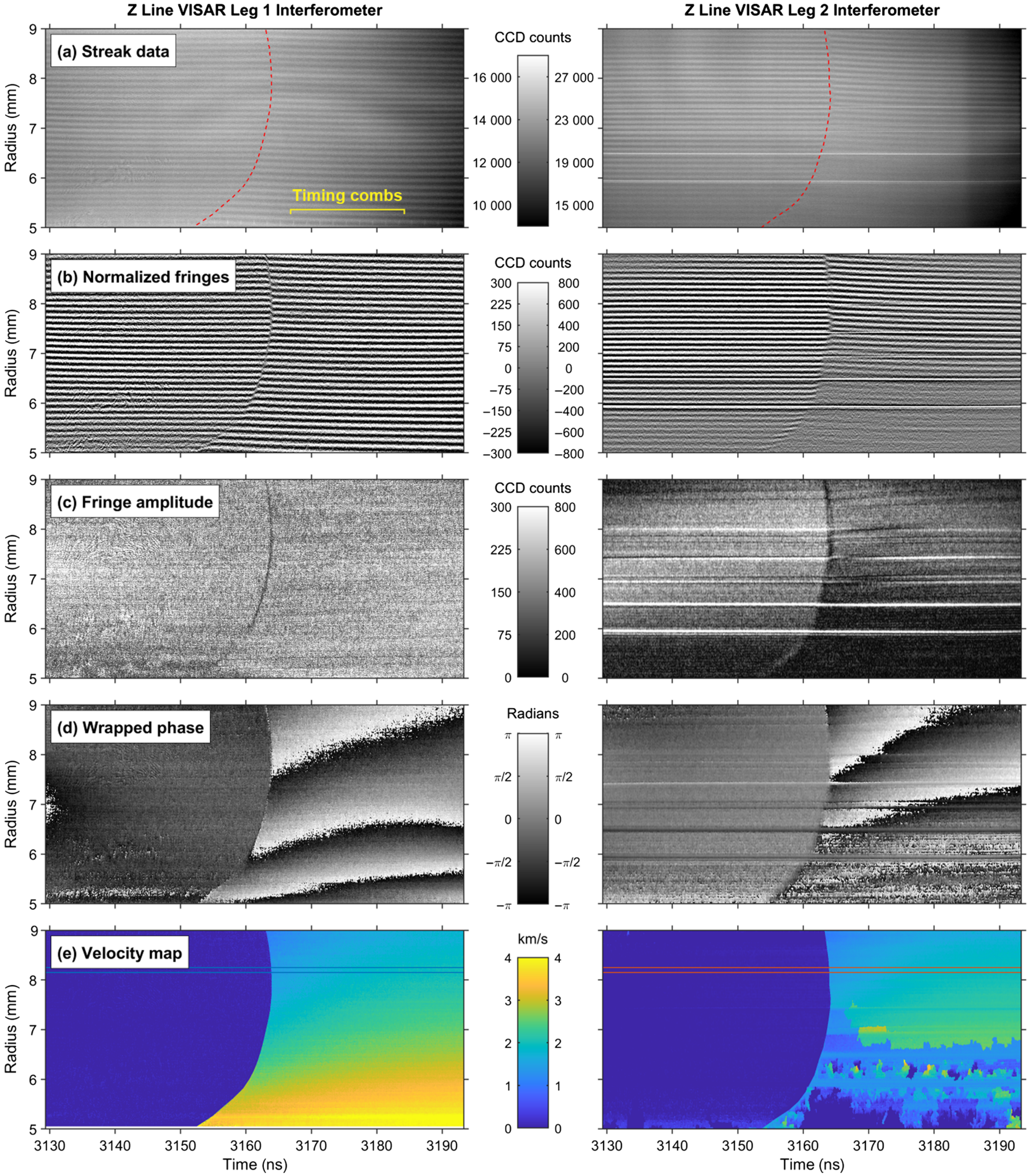

FIG. 7. Z Line VISAR interferograms and velocity analysis from the ZLV validation experiment (z3337). (a) Raw interferograms obtained from each ZLV interferometer leg. A curved shock breakout feature is highlighted in red in each image. Downward fringe motion is visible after shock breakout indicating that the top flyer plate continues to accelerate throughout the experiment. (b) Normalized fringe patterns obtained by subtracting the low-frequency background from the raw interferograms. (c) Root-mean-square fringe amplitude identified by the Fourier transform method of Celliers *et al.* [36]. (d) Wrapped phase maps extracted after applying an inverse Fourier transform to the bandpass-filtered data. (e) Velocity maps obtained by unwrapping the wrapped phase maps, subtracting the linear phase ramp from the background fringe pattern, and applying the velocity per fringe (VPF) multiplier associated with the etalon that was fielded in each interferometer leg. See the text for further details.

Fig. 7(d) shows the wrapped phase maps obtained by applying an inverse transform to each of the bandpass filtered interferograms. Note that the postshock fringe amplitude on the lower half of Leg 2 is insufficient to extract meaningful phase information from that portion of the interferogram.

Figure 7(e) shows the final velocity maps obtained by unwrapping the phase maps in Fig. 7(d) and applying the VPFs listed in Table I. The Leg 1 map is clean everywhere except $R < 5.5$ mm where bright horizontal streaks appear in the data. These streaks are an artifact of the timing combs that are visible at the bottom of the raw Leg 1 interferogram in Fig. 7(a). For most subsequent ZLV experiments, the timing combs are recorded preshot and then removed for the downline experiment so as to avoid introducing such artifacts. The Leg 2 velocity map, on the other hand, only contains meaningful velocity information at a large radius ($R \gtrsim 7$ mm). This is due to the lack of fringe contrast in the bottom half of the Leg 2 interferogram. In spite of the lack of velocity data at a small radius on Leg 2, the data on the large radius side are crucial in that it permits the reconciliation of the fringe ambiguity that is introduced by the shock breakout feature in this experiment.

Fringe ambiguities are a well-known challenge in VISAR analysis that are encountered when large phase jumps, typically at shock fronts, discontinuously shift the fringes by more than the $[-\pi, \pi]$ range of the wrapped phase function. At such discontinuities, the phase can experience integer fringe shifts that are not resolved in the data, leading to ambiguity about the height of the shock in velocity space. The key to reconciling fringe ambiguities is to field different etalons (and therefore different VPFs) in the two ZLV interferometer legs. In this configuration, the final velocity map is only a valid solution if a set of integer fringe shifts applied to the data from each leg results in the same shock height on both velocity maps. This multietalon technique substantially reduces the set of possible solutions, with the remaining spurious solutions being far removed from the expected shock height as informed by preshot simulations. Note that constraining the fringe jump condition at a single radial location defines the jump condition for the full spatial range of the velocity map.

On the ZLV validation experiment, a fringe ambiguity is encountered at the shock front that extends across the 4 mm field of view [see Fig. 7(b)]. The two VPFs that were fielded (see Table I) permit the reconciliation of this fringe ambiguity. Figure 8 shows velocity lineouts from the two ZLV interferometer legs taken at $R \simeq 8.2$ mm. The location of these lineouts corresponds to the blue and red horizontal lines in the left and right panels of Fig. 7(e), respectively. Multiple versions of each lineout are shown in Fig. 8, each with a different number of integer fringe jumps applied at the time of shock breakout. Two possible self-consistent solutions are identified, one of which is labeled as the selected match and the other as an alternate match. We know from the simulations presented in Sec. IV and the point probe data presented in Sec. VI that the velocity at $R \simeq 8.2$ mm is unlikely to exceed 2 km/s, so we select the slower of the two possible solutions. Note that the velocity maps shown in Fig. 7(e) already include the integer fringe jump correction identified in Fig. 8. The successful reconciliation of the fringe ambiguity on the ZLV validation experiment illustrates the importance of having obtained velocity data from both interferometer legs even if the small-radius part of the Leg 2 velocity map could not be unfolded.

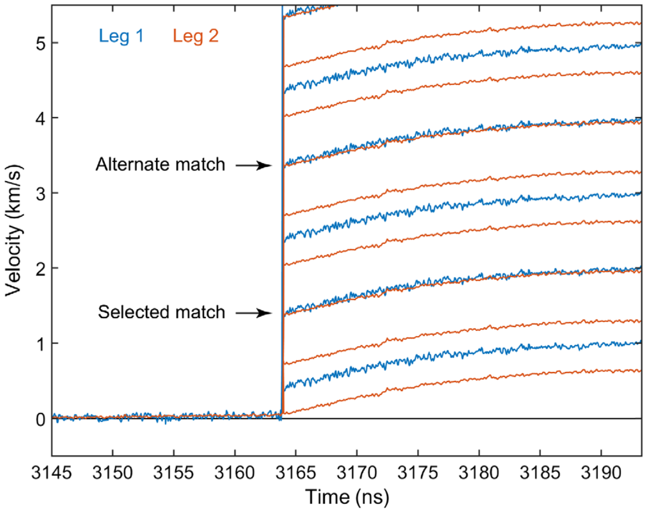

FIG. 8. Fringe ambiguity reconciliation on the ZLV validation experiment. The velocity lineouts shown here are extracted from the Leg 1 and Leg 2 velocity maps at $R \simeq 8.2$ mm as indicated by the respective blue and red horizontal lines in Fig. 7(e). Multiple versions of each lineout are shown, each with a different number of integer fringe shifts applied at the time of shock breakout. The selected match between the two lineouts, which is informed by the simulations presented in Sec. IV and the point probe data presented in Sec. VI, is the fringe jump condition that is applied to the velocity maps in Fig. 7(e). See the text for further details.

With the Leg 1 velocity map in hand, the remaining task is to determine what the measured velocities can tell us about the current delivered across the underside of the top flyer plate on the ZLV validation experiment. To this end, Sec. IV compares the experimentally measured velocities to the results of 2D simulations from four different magnetohydrodynamic codes. These comparisons demonstrate that the Leg 1 velocity map is consistent with lossless current delivery across the top flyer plate. Additionally, Sec. V presents direct current unfolds generated from the return can and ZLV velocity data. These unfolds inform what can and cannot be quantitatively determined about current delivery from line VISAR velocity data. For the analysis presented in Secs. IV and V, it is important to identify the uncertainty in the Leg 1 velocity map. With line VISAR data, it has been shown that typical uncertainties are ±5% of the VPF [36]. This VPF-based uncertainty, which for

Leg 1 on z3337 is ±50 m/s, often dwarfs the rms (root-mean-square) noise floor of the interferograms. For the ZLV validation experiment, however, where the fringe amplitudes were undesirably low, the rms noise floor is ±50 m/s for $R > 5.5$ mm and ±100 m/s for $R < 5.5$ mm where the timing combs are located. Combining the VPF and rms uncertainties in quadrature gives $\delta v \sim \pm 70$ m/s for $R > 5.5$ mm and $\delta v \sim \pm 110$ m/s for $R < 5.5$ mm. These velocity uncertainties, which constitute a ±3–7% error bar, will be used to inform the current delivery analysis presented in Secs. IV and V.

IV. TWO-DIMENSIONAL SIMULATION COMPARISONS

In this section, we compare the experimentally measured ZLV Leg 1 velocity map in Fig. 7(e) to 2D simulation results from four different magnetohydrodynamic (MHD) codes. The purpose of this exercise is to demonstrate that multiple MHD codes generate top-flyer-plate velocity maps that are essentially identical to each other and to the experimentally measured Leg 1 velocity map. This cross comparison confirms that both the ZLV diagnostic and the MHD codes are working well in this regime and that the current delivery across the top flyer plate was indeed lossless on the ZLV validation experiment.

The four MHD codes used here are Hydra, Gorgon, Alegra, and Ares. Hydra is a 2D and 3D multimaterial arbitrary Lagrangian-Eulerian (ALE) radiation hydrodynamics code [61] with a resistive MHD package that enables the simulation of magnetic direct drive inertial fusion experiments [62,63]. Gorgon is a 2D and 3D Eulerian resistive MHD code [10,64,65] that has been adapted by Sandia National Laboratories to simulate a variety of magnetically driven Z-pinch experiments at the Z Pulsed Power Facility [10,66–68]. Alegra is an ALE remap multiphysics code that includes material strength and the MHD approximation [69]. It has been benchmarked across a variety of applications at the Z Pulsed Power Facility, including dynamic materials properties experiments [18] that utilize the same key physics that is required to model the ZLV validation experiment. Finally, Ares is a single-fluid, multicomponent, multimaterial ALE radiation hydrodynamics code [70–72] that has resistive [73] and Hall [74] MHD packages that can be employed in pulsed-power simulations. Each code uses a pair of the material equation of state (EOS) and electrical conductivity (ECON) tables to model the response of the copper top flyer plate to the Z current pulse. Here, all four simulations use the Sesame 3325 EOS table [75] and one of two Lee-More-Desjarlais (LMD)-based ECON tables: the Hydra, Gorgon, and Ares simulations each use Sesame 29235 [76], while the Alegra simulations use the newer table of Porwitzky *et al.* [77].

Figure 9 compares 2D simulation results from the four different MHD codes to the velocity map measured by the ZLV Leg 1 interferometer on z3337. Each simulation implements a 2D *R-Z* representation of the load region (see Fig. 1b), the boundary of which is driven by the load current waveform that is unfolded from the return-can velocimetry measurements acquired at $R = 13$ mm. The details of the velocimetry unfold procedure and the resulting load current waveform that is used to drive the 2D simulations will be addressed in Sec. V and Fig. 10. The simulation results presented in Fig. 9 are as follows: The left column shows the simulated top flyer plate velocities on the same axes and color scale as the ZLV Leg 1 velocity map in Fig. 7(e). The experimentally measured shock breakout trajectory is shown as a red line on each of the simulated velocity maps in the left column of Fig. 9. Note that the simulated shock breakout curves each follow the same trajectory that is observed in the experiment. The timing of shock breakout in the simulations is set by the timing of the return-can-based input current waveform, meaning that no artificial timing adjustments have been made to the simulations.

The right column of Fig. 9 shows the difference between the simulated velocity maps and the experimental measurements. Since the simulated velocities are so similar to the experiment, the color scale in the right column spans just ±10% of the color scale in the left column. The differential velocity plots in the right column indicate that the temporal shock breakout profile is sharper in the experiment than in most of the 2D simulations. This is a result of the limited spatial resolution of the simulations and not a loss of physics fidelity. The key conclusions from the multicode comparison shown in Fig. 9 are as follows: First, the postshock velocities generated by the four codes are in remarkable agreement with each other. Each differential velocity plot in the right column shows the same pattern, indicating that the simulations are in agreement at the ±20 m/s level. This cross-code agreement builds confidence in our ability to simulate nonuniformly driven flyer plates using a range of numerical tools. The second key conclusion from Fig. 9 is that the simulations generate velocity maps whose mean postshock velocities agree with the experimental measurements to approximately the 70 m/s uncertainties of the ZLV data. The mean and standard deviation of the postshock differential velocities within the magenta outline are listed on each plot in the right column of Fig. 9. This level of agreement between simulation and experiment indicates that, within the ±3–7% uncertainty of the ZLV velocity data, the current delivery across the underside of the top flyer plate is lossless on the ZLV validation experiment. While this was the intended result of the experiment, these results serve as a quantitative validation both of the performance of the ZLV diagnostic and of our ability to model the experiment.

V. LOAD CURRENT UNFOLDS

With the conclusion that current delivery across the top flyer plate on the ZLV validation experiment is lossless and

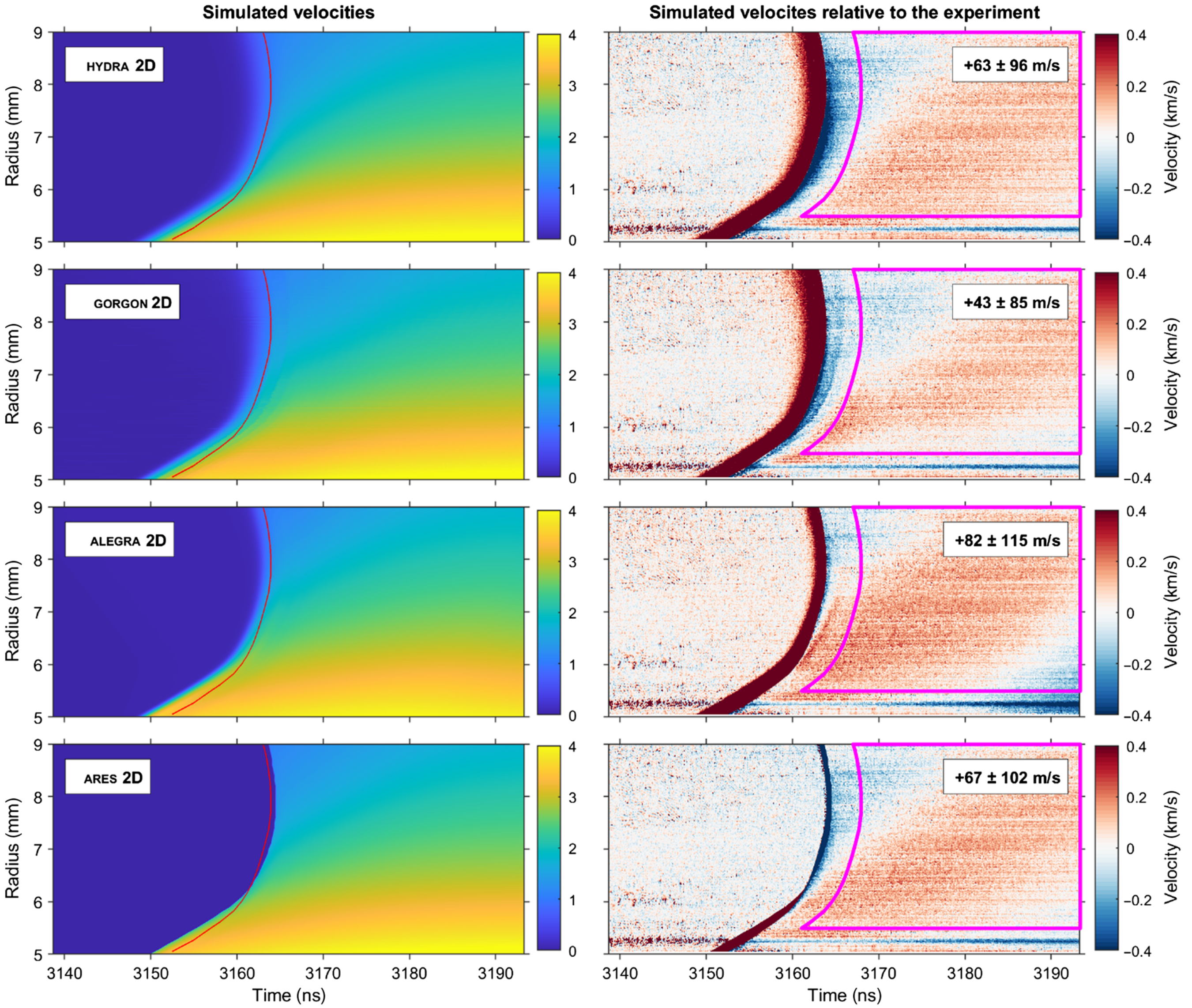

FIG. 9. Comparison of the velocities generated by 2D simulations from four magnetohydrodynamic codes to the experimentally measured ZLV Leg 1 velocity map. Each row in the figure presents the simulated top flyer plate velocities from one of the four codes (left) and the difference between the simulated velocities and the experiment (right). The red line on each of the velocity maps in the left column represents the experimentally observed shock breakout trajectory. Note that the color scale in the right column spans just ±10% of the color scale in the left column. Each plot in the right column lists the mean and standard deviation of the differential velocities in the postshock region outlined in magenta. The $R < 5.5$ mm region is excluded from this calculation due to the presence of timing combs in the raw interferogram. See the text for further details.

that the MHD codes are working well in this regime, we can now take the analysis a step further and use 1D MHD simulation tools to directly unfold the shape and amplitude of the load current pulse from the experimental velocimetry measurements. In this section, we first introduce the load current unfold procedure of Jennings [22] using the return-can point-probe-based velocity measurements as an example. Note that the resulting return-can current waveform is what was used to drive the 2D MHD simulations in Sec. IV. We then proceed to apply the same load current unfold procedure to the ZLV velocity data acquired at multiple radial locations. This analysis directly evaluates the current delivered across the top flyer plate as a function of radius and time, and it crucially quantifies the regions of validity and the uncertainties of each unfolded current waveform.

A. Return-can current unfolds

As described in Sec. II, the velocity history of the exploding return can flyer plate is measured on the ZLV validation experiment by point velocimetry probes that couple to both the PDV and VISAR systems at Z. Note that

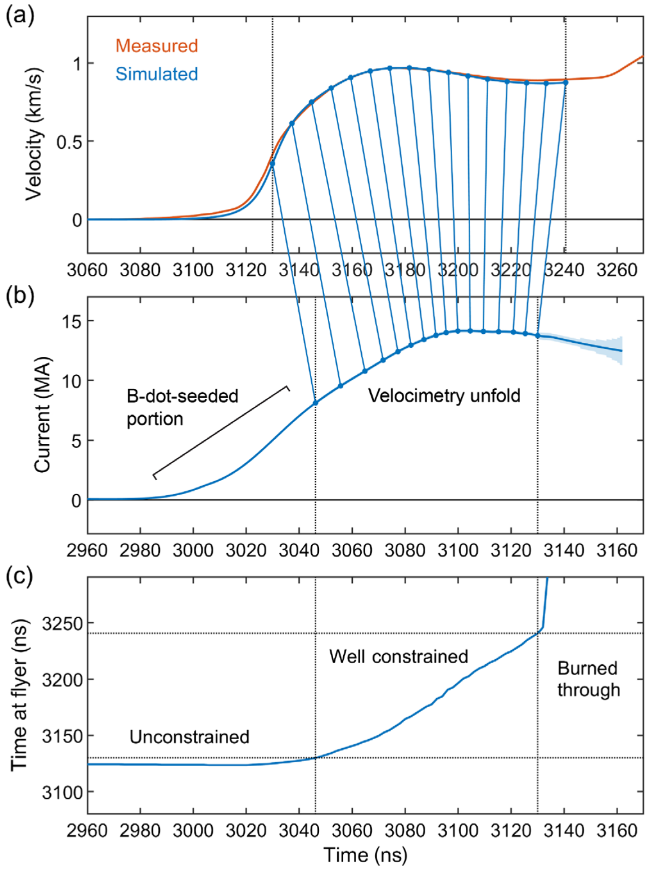

FIG. 10. Load current velocimetry unfold from the return can on the ZLV validation experiment. (a) Comparison of the return can flyer velocity history measured by PDV and VISAR (red) and the simulated velocity history generated by the converged current unfold (blue). (b) The converged current waveform unfolded from the measured velocity history. The light blue envelope around the dark blue current waveform represents the level of current perturbation that is constrained by the velocity data at each point in time. Note that the velocity time axis in (a) is shifted later relative to the current time axis in (b) due to the transit time through the flyer. Lines connecting velocity points in (a) to current points in (b) indicate the transit time of the magnetically driven pressure wave through the 400 μm-thick return can flyer. (c) The transit time mapping between the current drive on the inner surface of the return can and the velocity at the outer flyer surface. This relationship is used to determine the time period over which the velocity constrains the current. See the text for further details.

the fiber-coupled VISAR system is independent of the Z Line VISAR system. Figure 10 illustrates the process of unfolding the return can current from the point probe velocity data using the procedure developed by Jennings [22]. The underlying assumption is that the measured flyer plate velocities are directly correlated to the load current waveform because the flyer expansion is driven solely by the magnetic pressure generated by the load current. One of the most significant challenges with load current unfolds is that the velocity data do not constrain the current early in time due to the pileup of information in the initial pressure wave as it travels through the flyer. The velocity data also fail to constrain the current late in time because the information from late in the current pulse takes too long to propagate through the decompressing flyer. For the time in between, however, velocimetry is one of the most constraining load current measurements that can be made.

The unfold process begins by identifying a guess current waveform and then running a forward simulation with a 1D Lagrangian MHD code to model the flyer velocity that the guess current generates. Typically the guess current is derived from *B*-dot sensors that electromagnetically measure the current delivered to the Z vacuum chamber. While the guess current can differ substantially from the final load current unfold due to losses between the *B*-dot sensors and the load region as well as diagnostic uncertainties, the early-time shape of the *B*-dot-based guess current is similar enough to the final result to compensate for velocimetry's lack of sensitivity early in time. It is crucial that the shape of the early-time guess current approximate the final result because it can otherwise introduce unphysical oscillations in the flyer that pollute the unfolded current waveform. Once the flyer velocity generated by the guess current has been simulated, it is compared to the experimental measurements. The guess current (or more precisely the derivative of the guess current in the method of Jennings [22]) is iteratively refined until the simulated flyer velocity falls within the uncertainty of the experimental measurements. The specific iterative solver used here seeks to identify the minimum-curvature current pulse that satisfies the constraints of the velocimetry data.

Figure 10(a) compares the return can flyer velocity history measured by PDV and VISAR (red) to the simulated velocity history generated by the iteratively converged load current unfold (blue). Figure 10(b) shows the converged load current unfold itself (dark blue) along with an envelope (light blue) that represents the level of current perturbation that is constrained by the velocity data at each point in time. This current perturbation takes the form of a 4 ns ramp-and-hold increase or decrease in the current that is sustained for the duration of the current pulse. As such, the light blue envelope does not represent a traditional error bar, but rather the maximum perturbation amplitude (of the form described) that can be tolerated at a given point in time while keeping the resulting velocity within the constraints provided by the velocimetry data. The key to understanding the connection between the velocity data and the current waveform is the transit time mapping, which is shown in Fig. 10(c). This relationship captures how long it takes for information about the current drive on the inside of the return can to propagate through the return can flyer and emerge as a measurable velocity on the other side. Because larger currents launch faster-propagating pressure waves in the flyer, the details of the transit time map are specific to a given current waveform and current perturbation prescription. The transit time map shown in Fig. 10(c) has several key features that bracket the time period over which the velocity data constrain the load current. First, we see that any information about the current drive that was launched before $t \simeq 3045$ ns piles up and emerges from the flyer surface around $t \simeq 3130$ ns. This is because, up until this time, slowly propagating information from the foot of the current pulse is continuously being overtaken while still inside the flyer by more rapidly propagating information that was launched from later in the current pulse. As such, the velocity data on this experiment do not constrain the current pulse before $t \simeq 3045$ ns or equivalently before the current reaches $I \simeq 8$ MA. The early-time portion of the current waveform in Fig. 10(b) is provided by B-dot-based measurements of the current that is delivered to the final transmission line (shown in yellow in Fig. 1). This "B-dot-seeded portion" is blended with the unfolded current waveform by the iterative velocimetry solver.

Once the initial current drive information reaches the outer surface of the flyer at $t \simeq 3130$ ns, the transit time map in Fig. 10(c) shows that there is an extended phase where the velocity data provide a strong constraint on the load current waveform. More specifically, the monotonic ramp in the transit time shows that there is a one-to-one relationship between the velocity measured at the outer surface of the flyer and the current that was driving the inner surface of the flyer ~100 ns earlier. The transit time relationship during this well-constrained phase is further illustrated by the blue lines that connect points on the velocity waveform in Fig. 10(a) to points on the current waveform in Fig. 10(b). Note that the time axis in Fig. 10(a) is shifted later relative to Figs. 10(b) and 10(c) to account for the transit time through the flyer. Figure 10(c) shows that the well-constrained phase of the velocity history ends abruptly at $t \simeq 3240$ ns when the magnetic field from the current pulse "burns through" as it reaches the outer surface of the flyer. This leads to rapid changes in the material properties of the flyer and effectively ends our ability to correlate the measured velocity with the current drive. The good news is that, before burning through, the velocity history strongly constraints the current waveform over $t \simeq 3045$–3130 ns, which is an interval that extends ~30 ns past peak current.

The remaining component of the load current unfold procedure is to relate the uncertainties in the measured velocity history δv to the uncertainties in the unfolded current waveform δI. This serves both to quantify the uncertainties in the load current measurement and to provide a method for determining when to truncate the unfolded current pulse. The uncertainty quantification technique used here identifies, for each time in the current pulse, the largest ramp-and-hold current perturbation δI that can be applied from that time onward and still have the resulting flyer velocities stay within the δv of the measurement [22]. For the return can unfold in Fig. 10, the velocity uncertainty specified for the fiber-coupled PDV and VISAR diagnostics on Z is $\delta v \simeq 20$ m/s. This corresponds to a remarkably tight constraint on the current of $\delta I \simeq 150$ kA over the well-constrained portion of the current pulse ($t \simeq 3045$–3130 ns). Interestingly, the unfolded current waveform can be extended further by increasing the amplitude of the applied current perturbation. This technique works because the information from a larger perturbation will propagate more quickly through the flyer plate so that the same velocity data can constrain more of the current pulse, albeit with increased uncertainty. To this end, increasing the current perturbation to $\delta I \simeq 300$ kA, 600 kA, and finally 1200 kA allows us to extend the unfolded return-can current pulse in Fig. 10b from $t \simeq 3130$ ns out to 3160 ns. The progressively larger amplitude of the current perturbations is captured by the light blue envelope that surrounds the iteratively converged current waveform in Fig. 10(b). This converged waveform is what was used to drive the 2D MHD simulations in Sec. IV.

B. Top flyer plate current unfolds

With the 1D load current unfold procedure in-hand, we can now assess whether the same 1D unfold procedure can also be used to unfold a 2D radially resolved current map from the ZLV velocity data acquired from the top flyer plate. The key question is whether the radial evolution of the flyer is insignificant enough that the 1D MHD simulations that are used to drive the load current unfold machinery of Jennings [22] can replicate the 2D MHD simulations of the top flyer plate presented in Sec. IV. To answer this question, Fig. 11 compares two sets of 1D simulations to the 2D Eulerian GORGON simulations in Fig. 9. The 1D simulations in the top row of Fig. 11 are from a 1D version of the 2D GORGON code where the radial hydrodynamic and magnetic field links have been severed so that the same Eulerian code is available but only axial coupling occurs. This provides the cleanest isolation of the differences between 1D and 2D simulations. The result is that the 1D Eulerian simulations agree very well with the 2D results, indicating that the velocity gradients in the top flyer plate are not strongly coupled in 2D. Note that this conclusion is specific to this flyer plate and this current drive such that the quasi-1D behavior of the flyer would need to be reevaluated if, for example, the flyer thickness was changed or the current drive was increased.

The 1D simulations in the bottom row of Fig. 11 are from the 1D Lagrangian code that powers the load current unfold machinery of Jennings [22]. The 1D Lagrangian velocity map in Fig. 11 is generated by running an ensemble of 1D simulations at 10 μm increments across the $R = 5$–9 mm ZLV field of view. The two parameters that change from one simulation to the next are the flyer thickness [see Fig. 1(b)] and the magnetic pressure that drives the flyer [see Eq. (1)], both of which vary with radius. The

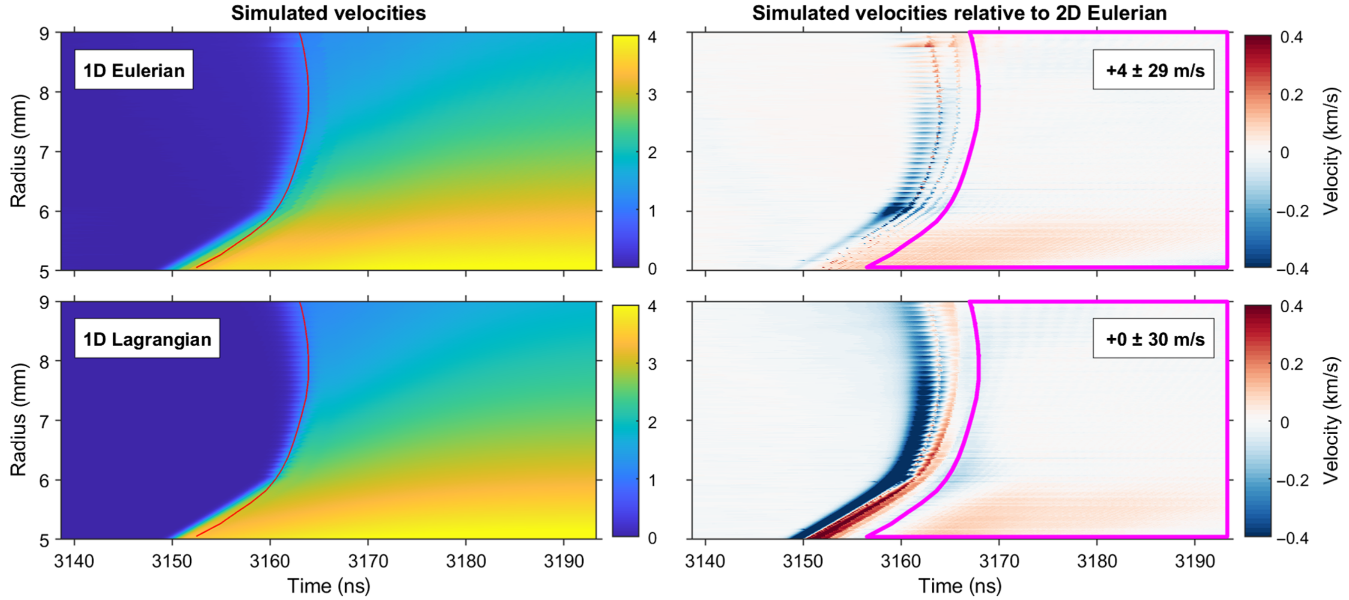

FIG. 11. Comparison of 1D Eulerian (top row) and 1D Lagrangian (bottom row) velocity maps to the 2D Eulerian GORGON velocity map in Fig. 9. The 1D Eulerian simulations are generated by severing the radial hydrodynamic and magnetic field links in GORGON. The 1D Lagrangian simulations are generated by running an ensemble of forward calculations within the current unfold machinery of Jennings [22]. As before, the red line in the left-hand column represents the experimentally measured shock breakout trajectory. The right-hand column shows the difference between the respective 1D and 2D velocity maps. The mean and standard deviation of the differential postshock velocities in the magenta region are listed for each case.

temporal evolution of the magnetic pressure is set by the load current unfold in Fig. 10(a). The resulting 1D Lagrangian velocity map in Fig. 11 is strikingly similar to the experimental data in Fig. 7(e) and to the 2D simulation results in Fig. 9. A quantitative comparison of the 1D simulated velocity maps in the left column of Fig. 11 to the 2D GORGON results is shown in the right column of Fig. 11.

The differential velocity maps in the right column of Fig. 11 indicate that the 1D and 2D simulations agree everywhere except in two regions: (i) along the shock breakout trajectory; and (ii) in the postshock region for $R < 6$ mm. The velocity differences along the shock breakout trajectory are caused by grid-scale artificial viscosity effects. While these effects blur the simulated shock front, they do not impact the postshock velocities. The differences in the postshock velocities in the $R < 6$ mm region are caused by a different effect: high radial velocity shear. Recall from Fig. 1(b) that the flyer is tapered over $R = 6$–10 mm so that the flyer thickness increases as the radius decreases to compensate for the increasing magnetic pressure at small radius. For $R < 6$ mm, however, the flyer has a constant thickness of 712.5 μm. This means that the radial velocity shear is larger in the $R < 6$ mm region than elsewhere and that the 1D simulations consequently have a more difficult time replicating the 2D results. This velocity shear effect emphasizes the importance of designing the radial profile of the flyer to minimize the radial velocity shear so that 1D load current unfold tools can still be used. Fortunately, in the ZLV validation experiment, the differences in the postshock velocities in the $R < 6$ mm region remain below the uncertainties in the experimental data, indicating that the 1D unfold machinery can be applied without a loss of fidelity.

To prepare the ZLV Leg 1 velocity map in Fig. 7(e) for unfold, an additional smoothing algorithm is applied. In general, we do not expect to need to smooth the ZLV data in order to extract the load current unfolds. However, the low fringe amplitudes and corresponding high noise floor on the ZLV validation experiment make generating a smoothed velocity map beneficial in this case. The smoothing algorithm applied here splits the velocity map in half at the shock front and smooths each half both parallel and perpendicular to the shock front. The resulting smoothed velocity map is shown in Fig. 12(a), and the difference between the smoothed map and the unsmoothed map from Fig. 7(e) is shown in Fig. 12(b). The latter plot confirms that the smoothing algorithm removes only the granular noise floor from the velocity map and does not alter the bulk velocities. Note that the smoothing algorithm also removes most of the artifacts generated by the timing combs in the $R < 5.5$ mm region of the map. Finally, Fig. 12(c) plots unsmoothed lineouts (in color) and the corresponding smoothed lineouts (black dashed lines) at roughly 0.5 mm increments across the ZLV field of view. The overall agreement between the smoothed and unsmoothed lineouts is evident. The smoothed lineouts in Fig. 12(c) are the velocity traces that are fed to the 1D load current unfold machinery.

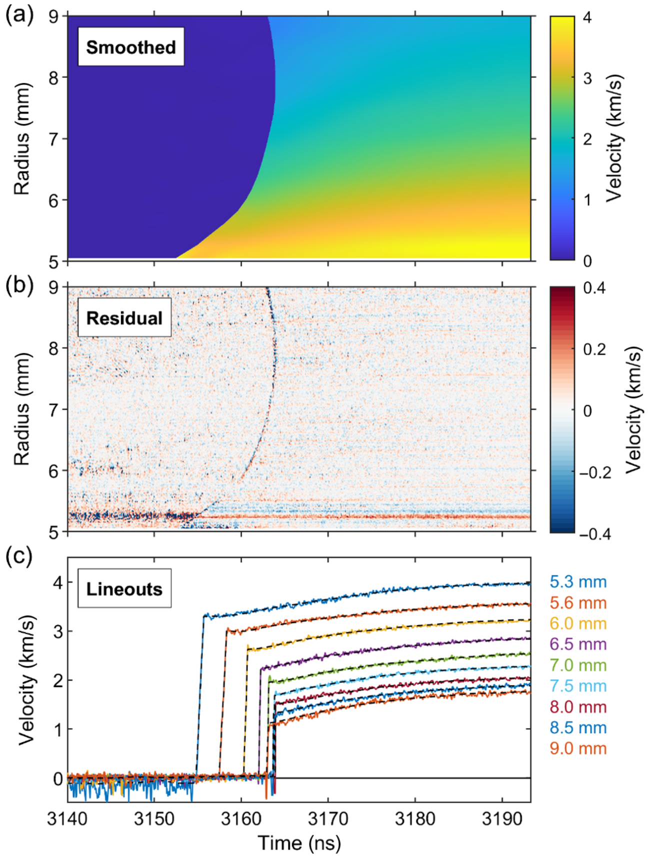

FIG. 12. (a) Smoothed velocity map generated from the unsmoothed ZLV Leg 1 velocity map in Fig. 7(e). (b) Difference between the smoothed velocity map and the unsmoothed map. Only the granular noise floor and artifacts from the timing combs are removed. (c) Comparison of smoothed lineouts (black dashed lines) and unsmoothed lineouts (in color). The smoothed lineouts are the velocity traces that are used for generating load current unfolds from the ZLV data.

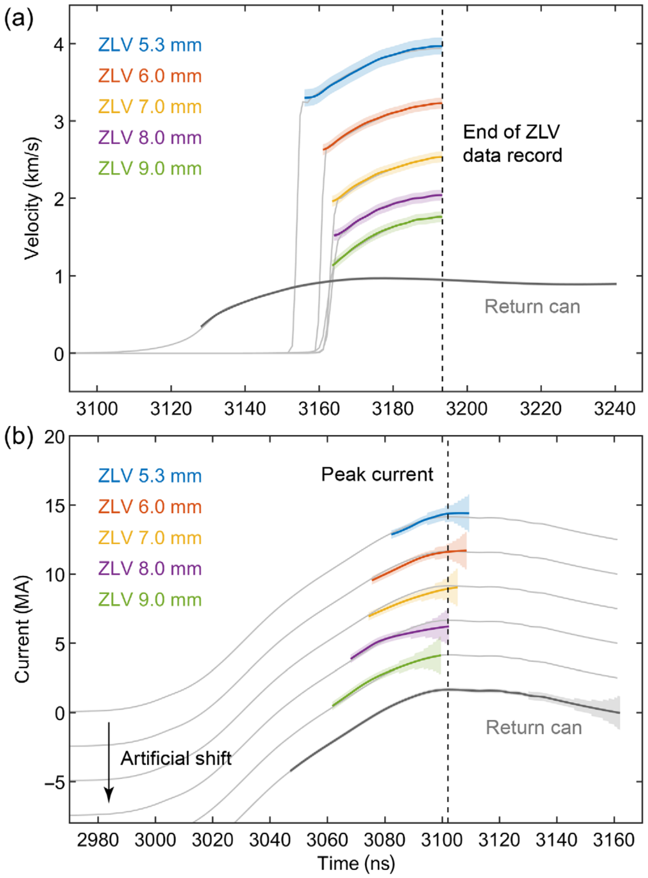

FIG. 13. 1D load current unfolds extracted from the ZLV velocity data. (a) Comparison of ZLV (color) and return can (gray) velocity lineouts showing that the ZLV streak camera substantially truncates the data record obtained from the top flyer plate. The light gray velocity traces at each radial location are simulated from the corresponding converged load current unfold. (b) Comparison of the load current unfolds from ZLV (color) and the return can (gray). An artificial vertical shift is applied to separate the various current unfolds for comparison. As with the return can unfold in Fig. 10(b), the lighter envelope around each unfold shows the level of current perturbation that is constrained by the velocity data. While the ZLV unfolds are constrained over a shorter period than the return can unfold, they provide key information about the portion of the current pulse leading up to and in most cases passing through peak current.

We now apply the same 1D load current unfold procedure that was used on the return can to unfold five top plate load current waveforms from the smoothed ZLV velocity lineouts extracted at the following radii: $R = 5.3$, 6.0, 7.0, 8.0, and 9.0 mm. Figure 13(a) compares the five ZLV velocity lineouts (in color) to the point probe velocity measurements from the return can [in gray, see Fig. 10(a)]. We immediately see that the ZLV velocity traces terminate well before the velocity trace from the return-can point probes. As described earlier in this section, the return-can point probe data are truncated when the magnetic field burns through the flyer. The ZLV data, on the other hand, are truncated when the data record ends on the Leg 1 streak camera. This illustrates that there is an inherent trade-off between the spatial and temporal resolution provided by ZLV and the dynamic record length provided by point velocimetry. Improvements in ZLV cross timing and experimental design on more recent ZLV experiments have extended the ZLV dynamic record from the 30–40 ns seen here to ~50 ns. In spite of these hardware-limited record lengths, ZLV's intrinsic value is that it can acquire spatially resolved velocimetry measurements from top flyer plate configurations that confound traditional point velocimetry (see Sec. VI for a direct comparison).

Returning to Fig. 13(a), the five ZLV traces in color represent the portion of each smoothed velocity lineout that is used to constrain the corresponding load current unfold. The lighter-colored envelopes around each lineout represent the velocity measurement uncertainties δv identified in Sec. III ($\delta v \sim \pm 70$ m/s for $R > 5.5$ mm and $\delta v \sim \pm 110$ m/s for $R < 5.5$ mm). The light gray velocity traces that are paired with each ZLV velocity lineout represent the simulated velocity generated by the corresponding load current unfold. As previously discussed, the breakout time and velocity amplitude observed at each radius are set by a combination of the current drive, the radial location, and the flyer thickness. It is clear that the unfold procedure is able to match these velocity variations when the appropriate radial location and flyer thickness information are provided to the 1D code.

Figure 13(b) shows the converged load current unfolds for each of the five ZLV lineouts (in color) and for the return can [in gray, see Fig. 10(b)]. An artificial vertical shift is applied to the various current traces in Fig. 13(b) to facilitate comparisons since they would otherwise overlap. For each ZLV current unfold shown in color, the return-can current unfold is repeated in light gray for comparison. We see that, due to the truncated nature of the ZLV velocity record, the portion of the current waveform that is constrained by the ZLV velocity data is substantially shorter than the portion constrained by the return can unfold. That being said, each of the ZLV unfolds constrains the crucial portion of the current waveform leading up to and, in the case of the smaller radii, passing through peak current. The time-dependent uncertainties δI for each of the ZLV unfolds are determined using the same ramp-and-hold perturbation technique described for the return can current unfold in Fig. 10(b). Here, the larger ZLV measurement uncertainties constrain the top plate load currents to an initial perturbation of $\delta I \simeq 300$ kA rather than $\delta I \simeq 150$ kA. The perturbation is increased in 150 kA increments to $\delta I \simeq 1.35$ MA before each ZLV unfold is truncated.

The key conclusion from Fig. 13(b) is that all five of the ZLV current unfolds overlay the return can unfold to within the uncertainty specified by the relevant δI envelope. This provides direct confirmation that current delivery across the top flyer plate on the ZLV validation experiment was indeed lossless, at least down to $R \simeq 5.3$ mm as constrained by the ZLV data. The peak current is constrained to $\delta I \simeq 600$ kA or $\sim 4\%$ at the two smallest radii. It is also interesting to note that the ZLV velocity information from the different radii constrains slightly different portions of the current waveform. The general trend is that the smaller radii begin constraining later because more current drive information piles up in the shock before breakout, but they also constrain the current longer because the information travels faster at smaller radii. In short, Fig. 13 provides the first demonstration that the ZLV diagnostic and 1D current unfold techniques can be used to quantify the current delivered across the top flyer plate on fast Z-pinch experiments at the Z Pulsed Power Facility.

VI. POINT PROBE COMPARISONS

A final point of comparison for the top flyer plate velocities measured by Z Line VISAR is to the traditional point velocimetry probes that were reflected onto the top flyer plate in the ZLV validation experiment as shown in Fig. 2. These top-down probes played a crucial role in the initial interpretation of the ZLV data in that they provided a coarse but trusted assessment of velocity versus radius on the top flyer plate. The quantitative utility of the top-down point probes is ultimately limited, however, because the throw distance from the probe tips to the mirror and then down to the flyer surface is atypically long (6–8 mm versus ~ 2 mm). The first consequence of the long throw distance is that random pointing errors with the fibers in each probe cause the probe spots to be projected at radii that are meaningfully different from the nominal locations of $R = 5$, 7, and 9 mm. The second and perhaps more insidious consequence of the long throw distance is that the spots that are projected onto the top flyer plate are 1–1.5 mm in diameter. Since the velocity varies substantially on millimeter scales, large-diameter probe spots capture a range of possible velocities with no ability to discriminate their spatial distribution.

The first step toward assessing the impact of finite spot sizes on the efficacy of the top-down point probes is to characterize the spot locations and sizes prior to the experiment. Figure 14 shows the characterization of the spots generated by the VISAR "send" fiber that transmits the VISAR laser to the flyer plate in each probe. Figure 14(a) illustrates the characterization procedure where a single fiber is backlit and projected onto a Kapton film located at the target height. The Kapton film is supported by an aluminum structure with cutouts of known dimensions. The light scattered off of the Kapton film is photographed, and the resulting image is analyzed to determine the radial position and diameter of the probe spot. Figure 14(b) shows the variation in the radial positions and diameters of the probe spots across the six top-down probes. Note that the two middle probes (nominally located at $R = 7$ mm) generate larger spot sizes because they are located above the other two probes in each triplet and therefore have a longer throw distance to reach the top flyer plate (see Fig. 2).

In spite of the long throw distance, the majority of the VISAR and PDV channels from the point probes returned signals that lasted at least through shock breakout in this experiment. The resulting velocity traces are qualitatively in the range of the ZLV velocity data, but making a quantitative assessment of current delivery from these traces is not possible. The reason is that the velocity that is recorded by the VISAR and PDV systems could be coming from anywhere within the cross section of the probe spots that are shown in Fig. 14(b). Given that the velocities can vary widely across the cross section of these probe spots, one cannot assign a single sensing radius from which the velocities are being recorded. The best way to illustrate this issue is to invert the problem and use the 2D MHD simulations from Sec. IV to determine the sensing radius where each probe was measuring the velocity as a function of time. To this end, Fig. 15 compares VISAR

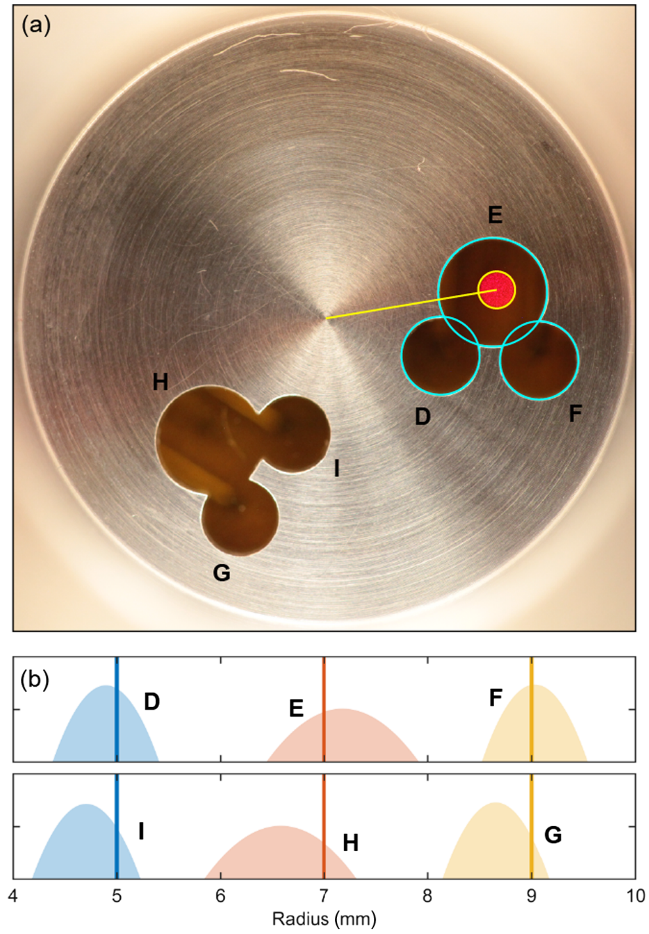

FIG. 14. Preshot characterization of top-down point probe spot sizes and locations on the z3337 load hardware. (a) Photograph of a backlit fiber on probe E (red) and the subsequent analysis (cyan and yellow lines) that is used to determine the radial location and diameter of the probe spot. (b) Characterization of the radial locations and spot diameters for the VISAR send fiber on each probe. Note that the radial locations often deviate meaningfully from the nominal values and that middle probes (E and H) have larger spot diameters due to the longer throw distance to the top flyer plate (see Fig. 2).

traces from one probe at each radial location to the 2D Hydra simulations from Sec. IV. Figure 15(a) plots one VISAR trace from each probe on top of the range of simulated velocities that occur within the cross section of the spot generated by the VISAR send fiber. Note that the range of velocities within the probe spot can reach ∼30% of the bulk velocity at small radius [in blue in Fig. 15(a)].

Figure 15(b) inverts the problem by determining the radius at which the measured velocities occur in the simulation as a function of time. We see that the sensing radius is not constant in time on any of the probes and that the signal is lost on the innermost probe when the sensing radius moves radially inward of the edge of the probe spot. This inward motion of the sensing radius is consistent with the shock front being tilted radially outward due to the local velocity shear. The tilted shock front preferentially reflects light from the inner side of the probe spot back into the probe. The evolution of the sensing radius shown in Fig. 15(b) is the fundamental reason why top-down point probes cannot be used to quantitatively assess current delivery on this experiment. This limitation serves to validate the importance of the line-imaging capability of the ZLV system, which enables spatially resolved measurements of the velocity that do not suffer from the sensing radius ambiguity shown in Fig. 15(b). We note here that subsequent diagnostic development with top-down point probes has shown that taking care to minimize the throw distance to the top flyer plate and using window materials such as lithium fluoride can improve the point probe data quality enough to generate an assessment of current delivery on similar experiments. That being said, the imaging capability of ZLV remains unmatched for assessing current delivery in the presence of large radial velocity shear.

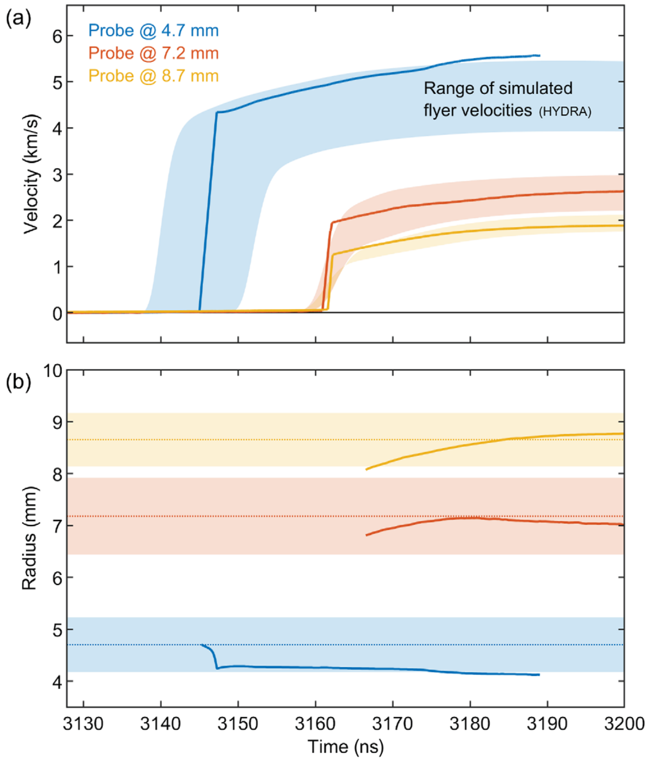

FIG. 15. Comparison of top-down point probe velocity to Hydra 2D simulations. (a) Overlay of one VISAR trace from point probes at each radial location on top of the range of simulated velocities within the characterized probe spot diameter. (b) Probe sensing radius versus time for each trace as determined by matching the measured velocities to the times and locations where these velocities occur in the simulations.

VII. SUMMARY AND DISCUSSION

In this paper, we report the first use of the Z Line VISAR diagnostic to acquire spatially resolved load current measurements at the Z Pulsed Power Facility. We describe the successful design and execution of a 14MA, 100 ns lossless experiment to validate both the performance of the ZLV diagnostic and our ability to model the results. Comparisons between the experimentally measured velocities and 2D simulations from four MHD codes indicate that current delivery on the ZLV validation experiment is lossless to within the few-percent uncertainties of the ZLV data. We proceed to establish that 1D current unfold techniques typically applied to return can velocimetry can also be used to directly extract load current waveforms from the ZLV velocity data. This remains the case so long as the radial velocity shear within the ZLV field of view is low enough that 1D simulations can capture the evolution of the top flyer plate. Finally, we compare the ZLV data to velocimetry measurements from top-down point probes to demonstrate that the finite spot sizes and lack of spatial discrimination in the point probes compromise their ability to tightly constrain the current delivered across the top flyer plate. These results validate the unique and transformative load current measurement capabilities provided by ZLV.

Improvements to the velocimetry setup and data quality on subsequent ZLV experiments are mentioned at several points in this paper. While the results of these follow-on experiments will be reported elsewhere, we note that additional tuning of the ZLV diagnostic following the validation experiment has greatly improved the spatial resolution and fringe contrast relative to this first experiment. One recent development that ensures uniform target illumination and robust postshock fringe tracking with ZLV is the use of aluminum-coated lithium fluoride (LiF) windows that are glued to the flyer surface. LiF windows also improve top flyer plate PDV data quality to the point that it serves as a useful complement to the ZLV measurements. These and other improvements have enabled the measurement of spatially resolved load current profiles on potentially lossy experiments with peak currents of $\gtrsim$20 MA.

The data that support the findings of this study are available from the corresponding author upon reasonable request.

ACKNOWLEDGMENTS

The authors thank the technical staff at the Z Pulsed Power Facility at Sandia National Laboratories and in the National Ignition Facility optical diagnostics group at Lawrence Livermore National Laboratory who contributed to the development, commissioning, and validation of the Z Line VISAR diagnostic. Sandia National Laboratories is a multimission laboratory managed and operated by National Technology & Engineering Solutions of Sandia, LLC, a wholly owned subsidiary of Honeywell International Inc., for the U.S. Department of Energy's National Nuclear Security Administration under Contract No. DE-NA0003525. This work was also performed under the auspices of the U.S. Department of Energy by Lawrence Livermore National Laboratory under Contract No. DE-AC52-07NA27344. This article describes objective technical results and analysis. Any subjective views or opinions that might be expressed in the article do not necessarily represent the views of the U.S. Department of Energy or the U.S. Government.

[1] D. B. Sinars, M. A. Sweeney, C. S. Alexander, D. J. Ampleford, T. Ao, J. P. Apruzese, C. Aragon, D. J. Armstrong, K. N. Austin, T. J. Awe *et al.*, Review of pulsed power-driven high energy density physics research on Z at Sandia, Phys. Plasmas **27**, 070501 (2020).

[2] M. E. Savage, K. R. LeChien, M. R. Lopez, B. S. Stoltzfus, W. A. Stygar, D. S. Artery, J. A. Lott, and P. A. Corcoran, Status of the Z pulsed power driver, in *Proceedings of 2011 IEEE Pulsed Power Conference, Denver, CO* (IEEE, New York, 2011), pp. 983–990, https://dx.doi.org/10.1109/PPC.2011.6191629.

[3] B. T. Hutsel, P. A. Corcoran, M. E. Cuneo, M. R. Gomez, M. H. Hess, D. D. Hinshelwood, C. A. Jennings, G. R. Laity, D. C. Lamppa, R. D. McBride *et al.*, Transmission-line-circuit model of an 85-TW, 25-MA pulsed-power accelerator, Phys. Rev. Accel. Beams **21**, 030401 (2018).

[4] A. Porwitzky, D. H. Dolan, M. R. Martin, G. Laity, R. W. Lemke, and T. R. Mattsson, Direct measurements of anode/cathode gap plasma in cylindrically imploding loads on the Z machine, Phys. Plasmas **25**, 063110 (2018).

[5] E. M. Waisman, M. P. Desjarlais, and M. E. Cuneo, Ion current losses in the convolute and inner magnetically insulated transmission line of the Z machine, Phys. Rev. Accel. Beams **22**, 030402 (2019).

[6] N. Bennett, D. R. Welch, C. A. Jennings, E. Yu, M. H. Hess, B. T. Hutsel, G. Laity, J. K. Moore, D. V. Rose, K. Peterson, and M. E. Cuneo, Current transport and loss mechanisms in the Z accelerator, Phys. Rev. Accel. Beams **22**, 120401 (2019).

[7] N. Bennett, D. R. Welch, G. Laity, D. V. Rose, and M. E. Cuneo, Magnetized particle transport in multi-MA accelerators, Phys. Rev. Accel. Beams **24**, 060401 (2021).

[8] T. C. Wagoner, W. A. Stygar, H. C. Ives, T. L. Gilliland, R. B. Spielman, M. F. Johnson, P. G. Reynolds, J. K. Moore, R. L. Mourning, D. L. Fehl *et al.*, Differential-output B-dot and D-dot monitors for current and voltage measurements on a 20-MA, 3-MV pulsed-power accelerator, Phys. Rev. ST Accel. Beams **11**, 100401 (2008).

[9] C. E. Myers, D. C. Lamppa, C. A. Jennings, M. R. Gomez, P. F. Knapp, M. R. Kossow, L. M. Lucero, J. K. Moore, and D. A. Yager-Elorriaga, The inductively driven transmission line: A passively coupled device for diagnostic applications on the Z pulsed power facility, Rev. Sci. Instrum. **92**, 033501 (2021).

[10] C. A. Jennings, M. E. Cuneo, E. M. Waisman, D. B. Sinars, D. J. Ampleford, G. R. Bennett, W. A. Stygar, and J. P. Chittenden, Simulations of the implosion and stagnation of compact wire arrays, Phys. Plasmas **17**, 092703 (2010).

[11] S. A. Slutz, M. C. Herrmann, R. A. Vesey, A. B. Sefkow, D. B. Sinars, D. C. Rovang, K. J. Peterson, and M. E. Cuneo,

Pulsed-power-driven cylindrical liner implosions of laser preheated fuel magnetized with an axial field, Phys. Plasmas **17**, 056303 (2010).

[12] M. R. Gomez, S. A. Slutz, A. B. Sefkow, D. B. Sinars, K. D. Hahn, S. B. Hansen, E. C. Harding, P. F. Knapp, P. F. Schmit, C. A. Jennings *et al.*, Experimental Demonstration of Fusion-Relevant Conditions in Magnetized Liner Inertial Fusion, Phys. Rev. Lett. **113**, 155003 (2014).

[13] M. R. Gomez, S. A. Slutz, C. A. Jennings, D. J. Ampleford, M. R. Weis, C. E. Myers, D. A. Yager-Elorriaga, K. D. Hahn, S. B. Hansen, E. C. Harding *et al.*, Performance Scaling in Magnetized Liner Inertial Fusion Experiments, Phys. Rev. Lett. **125**, 155002 (2020).

[14] C. A. Hall, J. R. Asay, M. D. Knudson, D. B. Hayes, R. L. Lemke, J. P. Davis, and C. Deeney, Recent advances in quasi-isentropic compression experiments (ICE) on the Sandia Z Accelerator, AIP Conf. Proc. **620**, 1163 (2002).

[15] R. W. Lemke, M. D. Knudson, D. E. Bliss, K. Cochrane, J.-P. Davis, A. A. Giunta, H. C. Harjes, and S. A. Slutz, Magnetically accelerated, ultrahigh velocity flyer plates for shock wave experiments, J. Appl. Phys. **98**, 073530 (2005).

[16] R. W. Lemke, M. D. Knudson, and J.-P. Davis, Magnetically driven hyper-velocity launch capability at the Sandia Z accelerator, Int. J. Impact Eng. **38**, 480 (2011).

[17] M. R. Martin, R. W. Lemke, R. D. McBride, J.-P. Davis, D. H. Dolan, M. D. Knudson, K. R. Cochrane, D. B. Sinars, I. C. Smith, M. Savage, W. A. Stygar, K. Killebrew, D. G. Flicker, and M. C. Herrmann, Solid liner implosions on Z for producing multi-megabar, shockless compressions, Phys. Plasmas **19**, 056310 (2012).

[18] R. W. Lemke, D. H. Dolan, D. G. Dalton, J. L. Brown, K. Tomlinson, G. R. Robertson, M. D. Knudson, E. Harding, A. E. Mattsson, J. H. Carpenter, R. R. Drake, K. Cochrane, B. E. Blue, A. C. Robinson, and T. R. Mattsson, Probing off-Hugoniot states in Ta, Cu, and Al to 1000 GPa compression with magnetically driven liner implosions, J. Appl. Phys. **119**, 015904 (2016).

[19] A. Porwitzky and J. Brown, Uncertainties in cylindrical anode current inferences on pulsed power drivers, Phys. Plasmas **25**, 063102 (2018).

[20] M. H. Hess, K. J. Peterson, D. J. Ampleford, B. T. Hutsel, C. A. Jennings, M. R. Gomez, D. H. Dolan, G. K. Robertson, S. L. Payne, W. A. Stygar, M. R. Martin, and D. B. Sinars, Design and testing of a magnetically driven implosion peak current diagnostic, Phys. Plasmas **25**, 042702 (2018).

[21] M. R. Gomez, S. A. Slutz, P. F. Knapp, K. D. Hahn, M. R. Weis, E. C. Harding, M. Geissel, J. R. Fein, M. E. Glinsky, S. B. Hansen *et al.*, Assessing stagnation conditions and identifying trends in magnetized liner inertial fusion, IEEE Trans. Plasma Sci. **47**, 2081 (2019).

[22] C. A. Jennings (private communication).

[23] L. M. Barker and R. E. Hollenbach, Laser interferometer for measuring high velocities of any reflecting surface, J. Appl. Phys. **43**, 4669 (1972).

[24] L. M. Barker, The development of the VISAR, and its use in shock compression science, AIP Conf. Proc. **505**, 11 (2000).

[25] J. R. Asay, L. C. Chhabildas, R. J. Lawrence, and M. A. Sweeney, *Impactful Times: Memories of 60 Years of Shock Wave Research at Sandia National Laboratories* (Springer, Cham, 2017).

[26] O. T. Strand, L. V. Berzins, D. R. Goosman, W. W. Kuhlow, P. D. Sargis, and T. L. Whitworth, Velocimetry using heterodyne techniques, in *26th International Congress on High-Speed Photography and Photonics*, SPIE Proceedings Vol. 5580 (SPIE-International Society for Optical Engineering, Bellingham, WA, 2005), pp. 593–599, https://dx.doi.org/10.1117/12.567579.

[27] D. H. Dolan, Extreme measurements with photonic Doppler velocimetry (PDV), Rev. Sci. Instrum. **91**, 051501 (2020).

[28] D. D. Bloomquist and S. A. Sheffield, Optically recording interferometer for velocity measurements with subnanosecond resolution, J. Appl. Phys. **54**, 1717 (1983).

[29] E. Moshe, E. Dekel, Z. Henis, and S. Eliezer, Development of an optically recording velocity interferometer system for laser induced shock waves measurements, Appl. Phys. Lett. **69**, 1379 (1996).

[30] W. F. Hemsing, A. R. Mathews, R. H. Warnes, and G. R. Whittemore, VISAR: line-imaging interferometer, in *Ultrahigh- and High-Speed Photography, Videography, Photonics, and Velocimetry '90*, SPIE Proceedings Vol. 1346 (SPIE-International Society for Optical Engineering, Bellingham, WA, 1991), pp. 133–140, https://dx.doi.org/10.1117/12.23342.

[31] K. Baumung, J. Singer, S. V. Razorenov, and A. V. Utkin, Hydrodynamic proton beam-target interaction experiments using an improved line-imaging velocimeter, AIP Conf. Proc. **370**, 1015 (1996).

[32] C. A. Hall, J. R. Asay, M. D. Knudson, W. A. Stygar, R. B. Spielman, T. D. Pointon, D. B. Reisman, A. Toor, and R. C. Cauble, Experimental configuration for isentropic compression of solids using pulsed magnetic loading, Rev. Sci. Instrum. **72**, 3587 (2001).

[33] M. D. Knudson, C. A. Hall, R. Lemke, C. Deeney, and J. R. Asay, High velocity flyer plate launch capability on the Sandia Z accelerator, Int. J. Impact Eng. **29**, 377 (2003).

[34] T. Ao, J. R. Asay, S. Chantrenne, M. R. Baer, and C. A. Hall, A compact strip-line pulsed power generator for isentropic compression experiments, Rev. Sci. Instrum. **79**, 013903 (2008).

[35] P. M. Celliers, G. W. Collins, L. B. Da Silva, D. M. Gold, and R. Cauble, Accurate measurement of laser-driven shock trajectories with velocity interferometry, Appl. Phys. Lett. **73**, 1320 (1998).

[36] P. M. Celliers, D. K. Bradley, G. W. Collins, D. G. Hicks, T. R. Boehly, and W. J. Armstrong, Line-imaging velocimeter for shock diagnostics at the OMEGA laser facility, Rev. Sci. Instrum. **75**, 4916 (2004).

[37] R. M. Malone, J. R. Bower, D. K. Bradley, G. A. Capelle, J. R. Celeste, P. M. Celliers, G. W. Collins, M. J. Eckart, J. H. Eggert, B. C. Frogget *et al.*, Imaging VISAR diagnostic for the National Ignition Facility (NIF), in *26th International Congress on High-Speed Photography and Photonics*, SPIE Proceedings Vol. 5580 (SPIE–International Society for Optical Engineering, Bellingham, WA, 2005), pp. 505–516, https://dx.doi.org/10.1117/12.579285.

[38] R. M. Malone, B. C. Frogget, M. I. Kaufman, T. W. Tunnell, R. L. Guyton, I. P. Reinbachs, P. W. Watts, J. R. Celeste,

P. M. Celliers, T. L. Lee, B. J. MacGowan, E. W. Ng, R. B. Robinson, and L. G. Seppala, Overview of the line-imaging VISAR Diagnostic at the National Ignition Facility (NIF), in *International Optical Design* (Optical Society of America, 2006), paper ThA5, https://dx.doi.org/10.1364/IODC.2006.ThA5.

[39] A. V. Mikhaylyuk, D. S. Koshkin, K. L. Gubskii, and A. P. Kuznetsov, Line-imaging VISAR for laser-driven equations of state experiments, J. Phys. Conf. Ser. **774**, 012057 (2016).

[40] W. M. Trott, M. D. Knudson, L. C. Chhabildas, and J. R. Asay, Measurements of spatially resolved velocity variations in shock compressed heterogeneous materials using a line-imaging velocity interferometer, AIP Conf. Proc. **505**, 993 (2000).

[41] M. R. Baer and W. M. Trott, Mesoscale descriptions of shock-loaded heterogeneous porous materials, AIP Conf. Proc. **620**, 713 (2002).

[42] W. M. Trott, M. R. Baer, J. N. Castañeda, L. C. Chhabildas, and J. R. Asay, Investigation of the mesoscopic scale response of low-density pressings of granular sugar under impact, J. Appl. Phys. **101**, 024917 (2007).

[43] C. A. Bolme and K. J. Ramos, Line-imaging velocimetry for observing spatially heterogeneous mechanical and chemical responses in plastic bonded explosives during impact, Rev. Sci. Instrum. **84**, 083903 (2013).

[44] M. K. Philpott, A. George, G. Whiteman, J. De'Ath, and J. C. F. Millett, The application of line imaging velocimetry to provide high resolution spatially resolved velocity data in plate impact experiments, Meas. Sci. Technol. **26**, 125204 (2015).

[45] J. Galbraith, K. Austin, J. Baker, R. Bettencourt, E. Bliss, J. Celeste, T. Clancy, S. Cohen, M. Crosley, P. Datte *et al.*, Design of a line-VISAR interferometer system for the Sandia Z Machine, in *Target Diagnostics Physics and Engineering for Inertial Confinement Fusion VI*, SPIE Proceedings Vol. 10390 (SPIE-International Society for Optical Engineering, Bellingham, WA, 2017), pp. 1–15, https://dx.doi.org/10.1117/12.2275088.

[46] P. Datte, J. Baker, D. Bliss, N. Butler, P. Celliers, S. Cohen, M. Crosley, J. Edwards, D. Erskine, D. Fratanduono *et al.*, The design of a line velocity interferometer for any reflector for inertial confinement experiments on the Z-machine, Rev. Sci. Instrum. **91**, 043508 (2020).

[47] M. D. Knudson, D. L. Hanson, J. E. Bailey, C. A. Hall, J. R. Asay, and W. W. Anderson, Equation of State Measurements in Liquid Deuterium to 70 GPa, Phys. Rev. Lett. **87**, 225501 (2001).

[48] D. G. Hicks, T. R. Boehly, P. M. Celliers, J. H. Eggert, S. J. Moon, D. D. Meyerhofer, and G. W. Collins, Laser-driven single shock compression of fluid deuterium from 45 to 220 GPa, Phys. Rev. B **79**, 014112 (2009).

[49] W. J. Nellis, Deuterium Hugoniot up to 120 GPa (1.2 Mbar), in *High Energy Density Laboratory Astrophysics*, edited by G. A. Kyrala (Springer Netherlands, Dordrecht, 2005), pp. 141–145, https://dx.doi.org/10.1007/1-4020-4162-4_20.

[50] Sydor Technologies, ROSS 5800 streak camera (2021), https://sydortechnologies.com/streak-cameras/ross-5800/.

[51] Sydor Technologies, Sydor DynaCal for ROSS 5800 streak camera calibration (2021), https://sydortechnologies.com/dynacal/.

[52] G. A. Fisk, G. A. Mastin, and S. A. Sheffield, Digital image processing of velocity-interferometer data obtained from laser-driven shock experiments, J. Appl. Phys. **60**, 2266 (1986).

[53] M. Takeda, H. Ina, and S. Kobayashi, Fourier-transform method of fringe-pattern analysis for computer-based topography and interferometry, J. Opt. Soc. Am. **72**, 156 (1982).

[54] K. A. Nugent, Interferogram analysis using an accurate fully automatic algorithm, Appl. Opt. **24**, 3101 (1985).

[55] J. B. Liu and P. D. Ronney, Modified Fourier transform method for interferogram fringe pattern analysis, Appl. Opt. **36**, 6231 (1997).

[56] S. Li, X. Su, and W. Chen, Spatial carrier fringe pattern phase demodulation by use of a two-dimensional real wavelet, Appl. Opt. **48**, 6893 (2009).

[57] M. Bahich, M. Afifi, and E. Barj, A numerical spatial carrier for single fringe pattern analysis algorithm, Optik (Stuttgart) **122**, 1821 (2011).

[58] D. Erskine, Speckle-adaptive VISAR fringe analysis technique, AIP Conf. Proc. **1793**, 160017 (2017).

[59] D. J. Erskine and D. E. Fratanduono, VISAR fringe analysis under extreme spatially varying conditions, AIP Conf. Proc. **1979**, 160006 (2018).

[60] D. J. Erskine, Forward modeling of Doppler velocity interferometer system for improved shockwave measurements, Rev. Sci. Instrum. **91**, 043103 (2020).

[61] M. M. Marinak, G. D. Kerbel, N. A. Gentile, O. Jones, D. Munro, S. Pollaine, T. R. Dittrich, and S. W. Haan, Three-dimensional HYDRA simulations of National Ignition Facility targets, Phys. Plasmas **8**, 2275 (2001).

[62] A. B. Sefkow, S. A. Slutz, J. M. Koning, M. M. Marinak, K. J. Peterson, D. B. Sinars, and R. A. Vesey, Design of magnetized liner inertial fusion experiments using the Z facility, Phys. Plasmas **21**, 072711 (2014).

[63] M. R. Weis, A. J. Harvey-Thompson, and D. E. Ruiz, Scaling laser preheat for MagLIF with the Z-Beamlet laser, Phys. Plasmas **28**, 012705 (2021).

[64] J. P. Chittenden, S. V. Lebedev, C. A. Jennings, S. N. Bland, and A. Ciardi, X-ray generation mechanisms in three-dimensional simulations of wire array Z-pinches, Plasma Phys. Controlled Fusion **46**, B457 (2004).

[65] A. Ciardi, S. V. Lebedev, A. Frank, E. G. Blackman, J. P. Chittenden, C. J. Jennings, D. J. Ampleford, S. N. Bland, S. C. Bott, J. Rapley, G. N. Hall, F. A. Suzuki-Vidal, A. Marocchino, T. Lery, and C. Stehle, The evolution of magnetic tower jets in the laboratory, Phys. Plasmas **14**, 056501 (2007).

[66] C. A. Jennings, J. P. Chittenden, M. E. Cuneo, W. A. Stygar, D. J. Ampleford, E. M. Waisman, M. Jones, M. E. Savage, K. R. LeChien, and T. C. Wagoner, Circuit model for driving three-dimensional resistive MHD wire array Z-pinch calculations, IEEE Trans. Plasma Sci. **38**, 529 (2010).

[67] T. J. Awe, C. A. Jennings, R. D. McBride, M. E. Cuneo, D. C. Lamppa, M. R. Martin, D. C. Rovang, D. B. Sinars,

S. A. Slutz, A. C. Owen *et al.*, Modified helix-like instability structure on imploding z-pinch liners that are preimposed with a uniform axial magnetic field, Phys. Plasmas **21**, 056303 (2014).

[68] C. A. Jennings, D. J. Ampleford, D. C. Lamppa, S. B. Hansen, B. Jones, A. J. Harvey-Thompson, M. Jobe, T. Strizic, J. Reneker, G. A. Rochau, and M. E. Cuneo, Computational modeling of krypton gas puffs with tailored mass density profiles on Z, Phys. Plasmas **22**, 056316 (2015).

[69] A. Robinson, T. Brunner, S. Carroll, R. Drake, C. Garasi, T. Gardiner, T. Haill, H. Hanshaw, D. Hensinger, D. Labreche *et al.*, ALEGRA: An arbitrary Lagrangian-Eulerian multimaterial, multiphysics code, in *46th AIAA Aerospace Sciences Meeting and Exhibit, Reno NV* (2008), https://dx.doi.org/10.2514/6.2008-1235.

[70] R. M. Darlington, T. L. McAbee, and G. Rodrigue, A study of ALE simulations of Rayleigh–Taylor instability, Comput. Phys. Commun. **135**, 58 (2001).

[71] B. Morgan and J. Greenough, Large-eddy and unsteady RANS simulations of a shock-accelerated heavy gas cylinder, Shock Waves **26**, 355 (2016).

[72] C. L. Ellison, H. D. Whitley, C. R. D. Brown, S. R. Copeland, W. J. Garbett, H. P. Le, M. B. Schneider, Z. B. Walters, H. Chen, J. I. Castor *et al.*, Development and modeling of a polar-direct-drive exploding pusher platform at the National Ignition Facility, Phys. Plasmas **25**, 072710 (2018).

[73] R. L. Masti, C. L. Ellison, J. R. King, P. H. Stoltz, and B. Srinivasan, Cross-code verification and sensitivity analysis to effectively model the electrothermal instability, High Energy Density Phys. **38**, 100925 (2021).

[74] W. A. Farmer, C. L. Ellison, and J. H. Hammer, Linear response of a Hall magnetic drift wave for verification of Hall MHD algorithms, Phys. Plasmas **26**, 072120 (2019).

[75] J. H. Carpenter (private communication).

[76] K. R. Cochrane, R. W. Lemke, Z. Riford, and J. H. Carpenter, Magnetically launched flyer plate technique for probing electrical conductivity of compressed copper, J. Appl. Phys. **119**, 105902 (2016).

[77] A. Porwitzky, K. R. Cochrane, and B. Stoltzfus, Determining the electrical conductivity of metals using the 2 MA Thor pulsed power driver, Rev. Sci. Instrum. **92**, 053551 (2021).